Abstract

Acknowledgements

Table of Contents

List of Tables

List of Figures

Chapter 1 - Introduction

1.1 Motivation and Objectives

Fossil fuels have traditionally been the main source of energy for power generation and transportation and it is anticipated that they will continue to be the main source for years to come. Combustion of fossil fuels not only generates heat, which can be converted into power, but also produces pollutants harmful to human health. Stringent regulations are forcing manufacturers of automobiles and power plants to reduce these emissions while there is also a requirement to increase power and decrease fuel consumption in these devices. These objectives lead to a requirement of improved combustion in these devices and it is believed that understanding the combustion process is an important step in this improvement.

In most practical applications, combustion takes place in a turbulent flow field. In recent years, a lot of effort has been placed on understand the underlying phenomenon in turbulent combustion processes. A tool that is becoming increasingly powerful in studying turbulent combustion is computer simulation of the processes involved. Recent efforts at Direct Numerical Simulations (DNS) of turbulent reacting flows in simple geometries have lead to improved understanding of these processes. Even with these recent advances, the subject of turbulent flow is not fully understood in itself and combustion within a turbulent flow field makes it more difficult to fully understand the physical processes involved. One reason for this is the wide range of length and time-scales that one has to deal with when studying turbulent combustion process, which

makes simulations extremely expensive in terms of computational effort. This limitation makes it impractical to apply DNS methods to practical combustion systems due to computational limitations. To overcome this limitation, the equations governing the flow are typically averaged and the information lost through averaging is accounted for with the use of models. One of the major motivations for this study is to improve combustion models available as part of the KIVA-3v (reference) modified at the Engine Research Center at the University of Wisconsin (reference). These combustion models will be applied mainly to Diesel combustion and to simpler flows like piloted jet flames for purposes of validating the models.

The objective of developing predictive combustion models is that they can be useful in designing efficient and clean combustion devices by performing relatively inexpensive CFD calculations rather than time-consuming and expensive practical experiments. Predictive combustion models may also be useful in understanding and interpreting combustion phenomena by visualizing results from combustion simulations.

A predictive combustion model must be able to represent the major physics of the combustion process. This representation is achieved by solving equations that govern the conservation of mass, species and energy. These equations are given as (Kuo, 1986):

$$\frac{\partial \rho}{\partial t} + \frac{\partial}{\partial x_i}\left(\rho u_i\right) = 0\,, \tag{1-1}$$

$$\frac{\partial}{\partial t}\left(\rho u_i\right) + \frac{\partial}{\partial x_j}\left(\rho u_i u_j\right) = -\frac{\partial p}{\partial x_i} + \rho g_i + \frac{\partial \tau_{ij}}{\partial x_j} \tag{1-2}$$

$$\frac{\partial}{\partial t}(\rho Y)+\frac{\partial}{\partial x_i}(\rho u_i Y)=\frac{\partial}{\partial x_j}\left(\frac{\mu_l}{\sigma_l}\frac{\partial Y}{\partial x_j}\right)+\dot{\omega} \tag{1-3}$$

Here, ρ is the density, u_i is the velocity vector, p is the pressure, g_i is the body force vector, τ_{ij} is the stress tensor, Y is the mass fraction of any species, μ_l is the laminar viscosity, σ_l the laminar Schmidt number, and $\dot{\omega}$ the source term due to chemical reaction. Two other equations that need to be solved are the energy conservation equation and the equation of state.

As noted earlier, these governing equations need to be averaged in most computations. Upon averaging the equations (1-1), (1-2), and (1-3), unknown terms are generated that need to be modeled. One requirement of a good model is that the physical processes being simulated and the term used to model the physics must be consistent with each other. Models for some of the unknown terms in these averaged equations are the topic of discussion in chapters 2 and 3.

Development of a combustion model is based on an understanding of the underlying physics. Some of the physical processes occurring in turbulent combustion and in Diesel engines that are important in the development of models presented in this study are discussed below.

1.2 Overview of Turbulent Combustion

The following description of turbulent combustion in general and combustion in Diesel engines is one of many possible interpretations of the complex events taking place during

the combustion process. This description is based on the author's understanding of the combustion process and other descriptions of the process (Kuo, 1986; Musculus *et al*., 1995; Lee, 1999; Peters, 2000).

In order for combustion to occur, fuel and oxidizer must mix at the molecular level before they can react. In a laminar flow, this mixing is dominated by molecular diffusion whereas in a turbulent flow field, this mixing is typically dominated by turbulence. It is believed that once a range of different size eddies has developed in a turbulent flow, strain and shear at the interface between the eddies enhance the mixing. Molecular mixing of fuel and oxidizer takes place at the interface between small eddies. Once the fuel and oxidizer are mixed at the molecular level, they may react if conditions are suitable. The rate at which they react is often linearly proportional to their concentrations and exponentially proportional to the temperature.

The above description of combustion leads to two extremes of combustion: reactions limited by kinetics (reactants are well-mixed) and those limited by mixing. In Diesel engines, the entire spectrum of combustion regimes can be found. In a diesel engine, liquid fuel is injected into a gaseous charge towards the end of the compression stroke. As the liquid fuel enters the cylinder, the spray interacts with the vapor mass already present in the cylinder, resulting in droplet collisions and break up. The fuel droplets exchange mass and momentum with the charge and generate a tremendous amount of turbulent kinetic energy near the spray. This spray-induced turbulence greatly enhances the mixing rates, thus shortening the mixing time scales and inducing high strain rates.

As the droplets are evaporating, they act as point sources of fuel vapor in the engine cylinder. The fuel air mixture formed immediately after the start of injection must auto-ignite. The conditions required for auto-ignition are generally not met at the time of injection, rather only after an ignition delay lasting several crank angles. During the ignition delay, complex chemical reactions take place, breaking the fuel molecules down into radicals and intermediates. This process continues until the temperature, pressure and species concentrations promote highly exothermic runaway kinetics. The time required to induce the rapid high temperature reactions varies throughout the cylinder.

During the ignition delay, a considerable amount of fuel vaporizes and mixes with the cylinder charge, thus forming a highly combustible mixture. Experimental evidence suggests that this mixture is fuel rich with an equivalence ratio between 2 and 4 (Dec, 1997). During the time in which ignition occurs, this fuel air mixture reacts quickly. This rapid consumption of the fuel air mixture prepared during the ignition delay is referred to as the premixed burn phase, and is responsible for the initial spike found in some heat release diagrams. As the turbulence and mixing rates are very large, the premixed reactions are typically kinetically limited. Thermal conduction in the high temperature ignition zones promotes ignition in neighboring fuel air mixtures. At this point, regions in the cylinder fall into two categories: 1) clusters of drops which have not ignited, where the fuel is vaporizing and mixing with the cylinder charge while participating in low temperature kinetics and 2) groups of droplets burning in a premixed fashion, with oxidizer being found between the droplets and the flame.

After some time, the oxidizer between the flame and the droplets is consumed and a diffusion flame forms at the jet periphery between the oxidizer and the incomplete combustion products (Dec, 1997). Fuel vaporizing from droplets within this diffusion flame must be transported to the reaction zone to find sufficient oxidizer to react. This diffusion burn is limited by the processes that vaporize droplets and transport fuel and oxidizer to the flame surface. During this mixing-limited diffusion burn, the flame surface is transported and stretched by the turbulent gases. Thus, the induced strain rates on the flame surface change drastically temporally and spatially. After some time, most of the premixed fuel is exhausted, and the remainder of the combustion process is limited by diffusion burn processes.

Representing the above physical description of the turbulent combustion process with models can be challenging given the complexity of the processes being modeled. The following section discusses some of the common combustion models used by various researchers.

1.3 Combustion Models

One of the simplest approaches to combustion modeling is to assume that reactions are kinetically limited and use rates of reaction as determined by chemical kinetics alone. The most commonly used rate expression is an Arrhenius type reaction rate (Brady *et al*., 1986). Reactions may be expressed as single step reactions where fuel and oxidizer are completely converted to products. In reality, the process of conversion of fuel and

oxidizer to products may involve thousands of elementary reactions steps. Another approach is to systematically reduce these elementary into a few global reaction steps and use these global reactions to represent the chemical kinetics.

Another simple modeling method assumes that the turbulent mixing rate dominates the combustion process. Such models are often referred to as eddy break up (EBU) models. This model was first proposed by Spalding (1971) who argued that chemical reactions are controlled by the cascade of energy from the large scales of motion to the small scales of motion and the rate of chemical reaction can be determined using information from large-scale quantities.

Since combustion in engines may lie between these two extremes, several different models have been used to model diesel combustion. One of these is a variation of the EBU model proposed by Magnussen *et al*. (1976). They combine a chemical time-scale with the mixing time-scale in a hybrid scheme. This model has been successfully applied to simulate diesel combustion in several studies.

Another widely used model is an extension of the characteristic time model (Abraham *et al*., 1985) to Diesel combustion (Kong *et al*., 1995). In this model, the rate of conversion of a species from is present state to the equilibrium state is assumed to occur at a characteristic time-scale. The characteristic time-scale is determined as a combination of a kinetic scale and a mixing time-scale. The kinetic time-scale is derived from a single

step reaction rate correlation for diesel fuel while the mixing time-scale is derived from turbulence quantities.

A separate approach to modeling of turbulent combustion is to separate the laminar chemistry from the turbulent flow field using the laminar flamelet model. An introduction to the laminar flamelet concept is presented in Chapter 3. A good review of the laminar flamelet concept and models that use this concept is presented by Peters (1984).

Several models that are based on the laminar flamelet concept have been used by researchers to model diesel combustion. One of these is a coherent flamelet model (Musculus *et al*., 1995). This model provides a transport equation for the density of the flame area. The overall reaction rate is then found by integrating the reaction rate per unit flame area for a strained laminar flame over all of the flame area.

Another model called the Representative Interactive Flamelet (RIF) Model developed by Barths *et al*. (1998) has been successfully used to simulate diesel combustion. This model uses the laminar flamelet concept with Probability Density Function (PDF) methods to accurately simulate processes such as ignition, premixed burn and diffusion burn. This complex model requires an unsteady diffusion flamelet solver to work together with the CFD code. Further, this model incorporates detailed chemical kinetics making the simulations are expensive in terms of CPU time usage.

Rogg *et al*. (1986) have applied the laminar flamelet model to partially premixed systems. In their model, a flamelet is characterized by the extent of stretching to which they are exposed and additionally by the degree to which it's reactants are premixed. Results from this model, which incorporates detailed kinetics, were shown to agree very well with experimental results.

1.4 Turbulence Modeling

It is known that turbulence is critical to the proper operation of an internal combustion engine (Heywood, 1988). The reason for this is that turbulent mixing rates are typically significantly larger than the molecular diffusion processes. The turbulent mixing will serve to increase the flame speed for premixed flames, typical of a spark ignited (SI) engine, and it will serve to enhance the oxidizer and fuel mixing rate in diffusion flames, typical of diesel engines. Thus, in order to accurately model the combustion process in an internal combustion engine the effects of turbulent mixing must be included. As noted earlier, current computational limitations are not enough to directly simulate all the length scales in a complex flow. Thus, a turbulence model is necessary to account for the effects of the unresolved scales.

The goal of turbulence modeling is to represent the physics of the flow as accurately as possible with as little computational expense as possible. In traditional approaches, the effects of turbulence have been modeled by adding a turbulent viscosity to the molecular viscosity in the momentum equation. It is reasoned that the primary effect of turbulence

is to increase mixing and therefore an effective turbulent viscosity can be used to simulate this effect.

One class of turbulence models is the Reynolds Averaged Navier-Stokes (RANS) models. In RANS models, the Navier-Stokes equations are ensemble averaged. This averaging process results in an extra stress term, the Reynolds stress, which is usually modeled with an effective turbulent viscosity. The ensemble averaging tends to remove the time-dependent part of the turbulent flow. In less complex flows, RANS models usually perform adequately; however, in more complex highly time-dependent flows such as an internal combustion engine, the ensemble averaging tends to smear out important structures in the flow field (Mellor and Ferguson, 1980) and therefore may be inappropriate (Libby and Williams, 1980). Thus, RANS models, such as $k-\varepsilon$, have significant drawbacks for use in modeling an internal combustion engine.

Another approach for modeling turbulence is large eddy simulation (LES). In the LES approach, the large scale eddies are solved for directly while the effects of smaller scale eddies are modeled. A property of a good LES model is that as the grid resolution approaches DNS, the effects of the sub-grid on the resolved scales are reduced and conversely as the resolution becomes coarser, the effects of the sub-grid on the resolved scale are increased. In conventional RANS models, there is no such mechanism in place to respond to the grid resolution.

To implement a LES model, the flow field must be separated into a large scale (resolved) and a small-scale (sub-grid) field (Pomraning, 2000). This is accomplished by using a filtering function, which is usually a local spatial average of the flow field. Thus, the resolved field can be solved for using the filtered time dependent Navier-Stokes equations while the effects of the small scales are accounted for through the additional stress terms that arise from filtering the time dependent Navier-Stokes equations. The ensemble averaging of the RANS models, which smears out flow structure, is replaced by local spatial averaging. By the nature of the LES averaging, unsteady flow behavior can be more accurately simulated. This makes LES methods more suited for complex highly time dependent flows such as in an internal combustion engine.

Typically, LES is computationally less expensive than DNS and computationally more expensive than RANS models. The main reason for this is that traditional LES requires that more scales of turbulence be resolved than RANS models yet it does not require that all of the scales of turbulence be resolved. Thus, an LES grid is typically denser than a RANS grid and less dense than a DNS grid. With recent increases in computational power, it has become feasible to use denser grids and therefore LES for complex engineering flows is more practical.

A number of LES models have been proposed by researchers. Some of these models were implemented into the KIVA code in this study and a discussion of these models along with a review of LES concepts is presented in Chapter 2.

LES methods have also recently been used to simulate simpler reacting flows. It is reasoned that simulations of simpler flows such as reacting jet flows and simulations of decaying isotropic turbulence of a reacting mixture will provide insight into the physics of combustion and turbulence-chemistry interactions. Since complex phenomena such as two-phase flow, evaporation and liquid-gas interactions that are present in IC engines do not occur in these flows, they provide detailed insight into both the combustion process and the behavior of the models themselves.

Pitsch (2000) has performed an LES of a reacting methane-air jet flame using an extended flamelet model. A lagrangian flamelet model (LFM) was used to simulate the Sandia series of flames (Barlow *et al*., 1998). The simulation results were in good agreement with the experiment indicating that the combustion model with LES was suitable for non-premixed combustion.

Cook *et al*. (1997) have applied a large-eddy probability density function combustion model to a reacting system of homogeneous, isotropic, decaying turbulence. Their comparisons of model results with filtered DNS data indicates that the model is reasonably accurate and that accuracy increases with increasing Damköhler number.

In conclusion, it seems that LES methods combined with flamelet models are promising methods for modeling turbulent, unsteady, reacting flows. LES and flamelet models developed in this study are presented in the following chapters.

Chapter 2 - Turbulence Modeling with Large Eddy Simulation

2.1 Introduction

The discussion in Chapter 1 indicated that LES methods might be well suited for simulations of internal combustion engines. Application of LES models to IC engine simulations is a relatively new field of research. Some work in this area has been carried out by Celik *et al*. (1998) who used LES methods to model flow and combustion in an internal combustion engine.

Four LES turbulence models have been implemented into the KIVA code: a zero-equation model (Smagorinsky, 1963), a one-equation viscosity based model (Menon *et al.*, 1996), a zero-equation dynamic Smagorinsky model (Germano, 1991), and a Dynamic Structure Model (Pomraning, 2000). In this chapter, a brief background of LES is first presented. This is followed by a discussion of aspects of some LES models that are important for modeling combustion.

2.2 Large Eddy Simulation Background

The LES decomposition of any flow variable ϕ is given as (Pomraning, 2000):

$$\phi = \bar{\phi} + \phi' . \tag{2-1}$$

The resolved quantity $\bar{\phi}$ is given by

$$\bar{\phi}(\mathrm{x}) = \int_V G(\mathrm{x},\mathrm{y})\phi(\mathrm{y})d\mathrm{y} , \tag{2-2}$$

where $G(x,y)$ is a spatial filter function that must satisfy

$$\int_V G(x,y)dy = 1, \tag{2-3}$$

for the flow variable to be conserved. Commonly used filtering functions include the box and Gaussian filters. The resolved component is determined by solving filtered transport equations of mass, momentum, energy, and species conservation. The effect of the sub-grid variables must be modeled.

Some properties of LES filters are presented here. Unlike RANS averaging, for most LES filters,

$$\overline{\bar{\phi}} \neq \bar{\phi} \quad and \quad \overline{\phi'} \neq 0, \tag{2-4}$$

where ϕ is any flow variable. Second, also unlike RANS averaging, the filtering operation only commutes with differentiation for a uniform stationary grid (Ghosal, 1995). In other words,

$$\frac{\overline{\partial \phi}}{\partial x} = \frac{\partial \bar{\phi}}{\partial x}, \tag{2-5}$$

only for a uniform stationary grid.

Upon filtering the governing equations, unclosed terms are generated which need to be modeled. Models for these terms typically have a model coefficient that needs to be determined. There are two broad classifications of sub-grid scale models for the unclosed terms—universal coefficient models and dynamic models. The universal coefficient models, in general, require the user to specify the model coefficient based on the flow and/or grid resolution. The appropriate universal model coefficient is frequently determined by comparing numerical calculations to experimental data. In dynamic models, the model coefficient is dynamically determined as a function of space and time

from the resolved field. This approach is based on an assumed scaling between resolved and sub-grid scales, and a mathematical identity that arises. These models offer the advantage of not requiring *a priori* knowledge of the flow to set the flow coefficient. Models using the dynamic approach are reasonably successful and have become widely used.

To formulate a dynamic model a second filtering operation, which is designated the 'test' level filter, is required. The 'test' filter operation is defined in a similar manner as the 'grid' filter operation:

$$\widehat{u_i}(\boldsymbol{x}) = \int_V G_T(\boldsymbol{x}, \boldsymbol{y})\, u_i(\boldsymbol{y}) d\boldsymbol{y}, \tag{2.6}$$

where the filter width of the test filter is required to be greater or equal to that of the first filter. The use of this test filtering operation to develop a dynamic model will be presented later in this chapter.

2.3 LES Momentum Transport

In order to accurately model the combustion process, the effects of turbulent mixing must be modeled correctly. In order to accomplish this, the averaged Navier-Stokes equation for momentum must be solved. This is obtained by filtering the Navier-Stokes momentum equation and is given as (Pomraning, 2000):

$$\frac{\partial \overline{\rho}\widetilde{u}_i}{\partial t} + \frac{\partial\left(\overline{\rho}\widetilde{u}_i\widetilde{u}_j\right)}{\partial x_j} = \frac{-\partial \overline{P}}{\partial x_i} + \frac{\partial \overline{\sigma_{ij}}}{\partial x_j} - \frac{\partial \tau_{u_i u_j}}{\partial x_j}, \tag{2-7}$$

where the bar indicates filtering at the grid level and

$$\overline{\sigma_{ij}} = \mu\left(\frac{\partial \widetilde{u_i}}{\partial x_j} + \frac{\partial \widetilde{u_j}}{\partial x_i}\right) - \frac{2}{3}\mu\frac{\partial \widetilde{u_k}}{\partial x_k}\delta_{ij}, \tag{2-8}$$

$$\tau_{u_i u_j} = \overline{\rho}\left(\widetilde{u_i u_j} - \widetilde{u_i}\,\widetilde{u_j}\right), \tag{2-9}$$

and $\tilde{u}_i$ is the LES Favre averaged velocity defined by

$$\tilde{u}_i \equiv \frac{\overline{\rho u_i}}{\overline{\rho}}. \tag{2-10}$$

The sub-grid stress tensor, $\tau_{u_i u_j}$, must be modeled as it cannot be readily determined from the resolved field. A number of approaches have been used to model this term. The three approaches presented here are a zero equation model, a one-equation viscosity model, and the dynamic structure model.

2.3.1 Zero Equation Model

In the zero-equation model and the one-equation model presented later, the sub-grid stress tensor is modeled using a gradient approximation as:

$$\tau_{u_i u_j} = \nu_t \overline{S}_{ij}, \tag{2.11}$$

where the filtered rate of strain tensor is defined as:

$$\overline{S}_{ij} = \frac{1}{2}\left(\frac{\partial \tilde{u}_i}{\partial x_j} + \frac{\partial \tilde{u}_j}{\partial x_i}\right) \tag{2.12}$$

The zero-equation model (Smagorinsky, 1963) is the simplest of LES sub-grid models and it does not require any additional transport equations. In this model, the turbulent viscosity is related to known quantities as:

$$\nu_t = 2C_s\Delta^2\left|\overline{S}\right| \tag{2.13}$$

where Δ is a length scale taken to be the filter width (taken as the cube root of the cell volume in this study). The magnitude of the filtered rate of strain tensor is defined as:

$$\left|\overline{S}\right| = \left(2\overline{S}_{ij}\overline{S}_{ij}\right)^{1/2} \tag{2.14}$$

The parameter, C_s, is a user-specified coefficient that may vary significantly with space. Approximate values of the coefficient have been determined to be between 0.01 and 0.3 (Pomraning, 2000) depending on the grid resolution and flow configuration. Thus, modeling complex turbulent flows using the Smagorinsky model requires *a priori* knowledge of the flow to set C_s correctly. This is a critical weakness for complex flows where *a priori* knowledge of the flow may not be available to set the universal coefficient. In addition, for complex flows, it may not be possible to find a universal coefficient that is appropriate for the entire domain at all times.

2.3.2 One Equation Sub-Grid Model

It is reasoned that the modeling of equation (2.11) can be improved by adding a transport for the sub-grid scale kinetic energy. One such model was proposed by Menon *et al.* (1996). The modeled from of the sub-grid kinetic energy transport is written as:

$$\frac{\partial k}{\partial t}+\frac{\partial \widetilde{u_j} k}{\partial x_j}=\frac{\partial}{\partial x_j}\left(\frac{\nu_t}{\sigma_k}\frac{\partial k}{\partial x_j}\right)-\tau_{ij}\frac{\partial \tilde{u}_i}{\partial x_j}-\varepsilon \tag{2.15}$$

where the sub-grid kinetic energy is defined as:

$$k=\frac{\overline{\rho}}{2}\left(\widetilde{u_i u_i}-\tilde{u}_i\tilde{u}_i\right). \tag{2.16}$$

The sub-grid stress tensor is modeled as:

$$\tau_{ij}=-2\nu_{tk}\overline{S_{ij}}\,, \tag{2.17}$$

where the turbulent viscosity, ν_{tk}, is modeled as

$$\nu_{tk}=C_k k^{1/2}\Delta\,. \tag{2.18}$$

A model for dissipation of the sub-grid scale kinetic energy, ε, is given by

$$\varepsilon=C_\varepsilon\frac{k^{3/2}}{\Delta}. \tag{2.19}$$

The constants in the model are set to $C_k = 0.05$, $C_\varepsilon = 1.0$, and $\sigma_k = 1.0$ (Yoshizawa, 1985).

One weakness with both the zero-equation model and the one-equation model, proposed in equations (2.11) and (2.17) above, is the assumption that the sub-grid stress tensor scales with the rate of strain tensor. It can be shown that this assumption cannot be justified (Pomraning, 2000). Moreover, in general, viscosity closures show very little correlation with the actual sub-grid stress tensor (Pomraning, 2000). Instead of modeling the stress tensor with a viscosity, a new model has been proposed by Pomraning (2000) where an attempt is made to estimate the stress tensor directly.

2.3.3 Dynamic Structure Sub-Grid Model

In the dynamic structure mode, the model coefficient is determined dynamically as a function of space and time from the resolved field rather than using a universal coefficient. A dynamic model requires that the momentum equation be filtered a second time at the 'test' level. The 'test' filter needs to be equal in width or wider than the 'grid' or first filter. The second filtering operation results in a stress tensor at the test level, given by

$$T_{ij} = \widetilde{\overline{\rho} u_i u_j} - \widetilde{\overline{\rho}} \widetilde{u}_i \widetilde{u}_j , \tag{2-20}$$

where

$$\widetilde{u}_i = \frac{\widetilde{\overline{\rho} u_i}}{\widetilde{\overline{\rho}}} . \tag{2-21}$$

The grid level and test level stress tensors are related by the Germano Identity (Germano, 1991).

$$L_{ij} = T_{ij} - \widehat{\tau_{ij}}, \tag{2-22}$$

where the Leonard stress term, L_{ij}, is given by

$$L_{ij} = \widehat{\overline{\rho}\widetilde{u}_i\widetilde{u}_j} - \widehat{\overline{\rho}}\widetilde{\widehat{u}}_i\widetilde{\widehat{u}}_j. \tag{2-23}$$

The Leonard stress term can be determined from the resolved field. The Germano identity is useful because it relates the two unknown stress tensors to a known tensor.

In the dynamic structure model, the equation for the sub-grid stress tensor is given by (Pomraning, 2000)

$$\tau_{ij} = c_{ij}k, \tag{2-24}$$

and the equation for the test level stress tensor is given by

$$T_{ij} = c_{ij}K, \tag{2-25}$$

where the grid level and test level sub-grid kinetic energies are defined by

$$k = \frac{\overline{\rho}}{2}\left(\widetilde{u_i u_i} - \widetilde{u}_i\widetilde{u}_i\right), \tag{2-26}$$

and

$$K = \frac{1}{2}\left(\widehat{\overline{\rho}\widetilde{u}_i u_i} - \widehat{\overline{\rho}}\widetilde{\widehat{u}}_i\widetilde{\widehat{u}}_i\right). \tag{2-27}$$

The grid level sub-grid kinetic energy is determined from a transport equation, the modeled form of which is given by

$$\frac{\partial k}{\partial t} + \frac{\partial \widetilde{u}_j k}{\partial x_j} = \frac{\partial}{\partial x_j}\left(\nu\frac{\partial k}{\partial x_j}\right) - \tau_{ij}\widetilde{S}_{ij} - \varepsilon \tag{2-28}$$

Models for the unclosed terms in equation (2-28) are discussed by Pomraning (2000). These models were validated using DNS data.

The grid and test level sub-grid kinetic energies are related by the trace of the Leonard term in equation (2-23) as

$$K = \widehat{k} + \frac{1}{2} L_{ii} . \tag{2-29}$$

The tensor structure of the sub-grid stresses is obtained from the tensor coefficient c_{ij}, which is found using the Germano identity. It is assumed that the tensor coefficient is the same at both filter levels. Substituting the models for the stress tensors into the Germano identity gives

$$L_{ij} = K c_{ij} - \widehat{k c_{ij}} . \tag{2-30}$$

An algebraic form of the model is obtained by assuming that the tensor coefficient can be removed from the integral in equation (2-30) and solving for τ_{ij} which gives

$$\tau_{ij} = L_{ij} \left(\frac{2k}{L_{kk}} \right). \tag{2-31}$$

Thus, the dynamic structure LES model obtains the tensor structure of the sub-grid stresses from a tensor coefficient rather than from the resolved scale stress tensor. Additionally, it is reasoned that since the sub-grid kinetic energy is related to the trace of the sub-grid stress tensor then a model of this form will scale well at the two filter levels. For this reason, it is assumed that the tensor coefficient is the same at both filter levels.

2.4 LES Scalar Transport

Determination of the mean species fractions in the combustion model (Chapter 3) requires the mean mixture fraction, its variance, and the mean stretch rate. In order to obtain these quantities, transport equations are solved for the mean mixture fraction and sub-grid mixture fraction fluctuations. The filtered LES equation for the Favre-averaged mixture fraction, $\tilde{\xi}$, is given as (Pomraning, 2000):

$$\frac{\partial \bar{\rho}\tilde{\xi}}{\partial t}+\frac{\partial \bar{\rho}\widetilde{u_i}\,\tilde{\xi}}{\partial x_i}=-\frac{\partial \tau_{u_i\xi}}{\partial x_i}+\overline{\frac{\partial}{\partial x_i}D\rho\frac{\partial \xi}{\partial x_i}}, \tag{2-32}$$

where the sub-grid scalar-flux is given by

$$\tau_{u_i\xi}=\bar{\rho}\left(\widetilde{u_i\xi}-\widetilde{u}_i\,\tilde{\xi}\right), \tag{2-33}$$

which needs to be modeled. Currently, this term is modeled using a gradient approximation as:

$$\tau_{u_i\xi}=-\mu_s\frac{\partial \tilde{\xi}}{\partial x_i}, \tag{2-34}$$

where μ_s is a scalar transport coefficient. When using the zero-equation sub-grid stress model and the one-equation sub-grid stress model, the scalar coefficient may be determined as:

$$\mu_s=\frac{\nu_t}{\sigma_t}, \tag{2-35}$$

where σ_t is the turbulent Schmidt number and ν_t is determined from equations (2.13) or (2.18). When using the dynamic structure model, the scalar transport coefficient is determined as:

$$\mu_s=C_k\Delta k^{1/2}. \tag{2-36}$$

Here, Δ is the filter width of the grid-level filter.

The unclosed term in the species conservation equation **(3-1)**, τ_{u_iY}, is modeled in a similar fashion as:

$$\tau_{u_iY}=-\mu_s\frac{\partial \tilde{Y}}{\partial x_i}, \tag{2-37}$$

The combustion model also requires the mean stretch rate and the variance of the mixture fraction. In order to evaluate these quantities, a transport equation for the sub-grid mixture fraction fluctuations is solved. The modeled form of this equation is given by

$$\frac{\partial \Phi}{\partial t}+\frac{\partial \widetilde{u_i}\,\Phi}{\partial x_i}=-\frac{\partial \tau_{u_i\Phi}}{\partial x_i}+2\tilde{\xi}\frac{\partial \tau_{u_i\phi}}{\partial x_i}+\frac{\partial}{\partial x_i}\left(D\frac{\partial \Phi}{\partial x_i}\right)-\bar{\rho}\chi \tag{2-38}$$

where

$$\Phi=\bar{\rho}\left(\widetilde{\xi\xi}-\tilde{\xi}\tilde{\xi}\right), \tag{2-39}$$

$$\tau_{u_i\Phi}=\bar{\rho}\left(\widetilde{u_i\xi\xi}-\widetilde{u_i}\,\widetilde{\xi\xi}\right), \tag{2-40}$$

and

$$\chi=2D\left(\widetilde{\frac{\partial \xi}{\partial x_i}\frac{\partial \xi}{\partial x_i}}-\frac{\partial \tilde{\xi}}{\partial x_i}\frac{\partial \tilde{\xi}}{\partial x_i}\right). \tag{2-41}$$

For the zero-equation Smagorinsky model and the one-equation model, the sub-grid mixture fraction fluctuation dissipation rate, χ, is modeled as:

$$\chi=C_\chi D\frac{\Phi}{\Delta^2}. \tag{2.42}$$

Here, C_χ, is a model constant and D is the laminar diffusion coefficient.

In the dynamic structure model, the dissipation rate, χ, is modeled as:

$$\chi=\frac{\Phi}{L_\Phi}L_\chi, \tag{2-43}$$

where

$$L_\chi=2D\left(\widehat{\bar{\rho}\frac{\partial \tilde{\xi}}{\partial x_j}\frac{\partial \tilde{\xi}}{\partial x_j}}-\hat{\bar{\rho}}\frac{\widehat{\partial \tilde{\xi}}}{\partial x_j}\frac{\widehat{\partial \tilde{\xi}}}{\partial x_j}\right), \tag{2-44}$$

$$L_\Phi=\widehat{\bar{\rho}\tilde{\xi}\tilde{\xi}}-\hat{\bar{\rho}}\hat{\tilde{\xi}}\hat{\tilde{\xi}}, \tag{2-45}$$

and

$$\hat{\tilde{\xi}}=\frac{\widehat{\bar{\rho}\tilde{\xi}}}{\hat{\bar{\rho}}} \tag{2-46}$$

Methods for modeling the other unclosed terms in equation (2-38) are discussed by Pomraning (2000).

The mean stretch rate $\overline{\chi}$, given by averaging equation **(3-7)**, is:

$$\overline{\chi} = 2D\widetilde{\frac{\partial \xi}{\partial x_i}\frac{\partial \xi}{\partial x_i}}. \tag{2-47}$$

This is determined from equation (2-41) as:

$$\overline{\chi} = \chi + 2D\frac{\partial \tilde{\xi}}{\partial x_i}\frac{\partial \tilde{\xi}}{\partial x_i}, \tag{2-48}$$

It can be seen that as grid resolution increases, this term approaches the instantaneous stretch rate defined in equation **(3-7)**. This offers an improvement over RANS models, which are known to do a poor job of predicting $\overline{\chi}$ (Peters *et al.,* 1988).

Equation (2-38) is also used to determine the variance of the mixture fraction. The relation, $\widetilde{\xi'\xi'} = \widetilde{\xi\xi} - \tilde{\xi}\tilde{\xi}$, which is true in a RANS model is not valid for LES averaging since, in general, for LES, $\widetilde{\xi'} \neq 0$. However, the two quantities, $\widetilde{\xi'\xi'}$ and $\widetilde{\xi\xi} - \tilde{\xi}\tilde{\xi}$ have the same qualitative trend as they tend to be large in regions of large gradients. Therefore, it is assumed that the quantity $\widetilde{\xi\xi} - \tilde{\xi}\tilde{\xi}$ can be used in place of $\widetilde{\xi'\xi'}$ to determine the PDF of ξ. Knowing $\tilde{\xi}$ from equation (2-32), $\widetilde{\xi\xi} - \tilde{\xi}\tilde{\xi}$ from equation (2-38), and $\overline{\chi}$ from equation (2-48) allows us to determine mean species mass fractions using equation **(3-22)**.

In the future, the sub-grid scalar flux in equation (2-33) could be modeled in a manner that is consistent with the Dynamic Structure LES model. This method is presented here. A dynamic model for the sub-grid scalar flux would be of the form

$$\tau_{u_i\xi} = c_i \beta_\xi \tag{2-49}$$

where

$$\beta_\xi = \Phi^{1/2} (2k)^{1/2}. \tag{2-50}$$

It is reasoned that equation (2-50) will provide the right scaling on the sub-grid scalar flux in the same way as that for the sub-grid turbulent stresses. In order to determine the coefficient c_i dynamically, a model of the form

$$L_{u_i\xi} = \widehat{\overline{\rho}\widetilde{u_i}\widetilde{\xi}} - \widehat{\overline{\rho}}\widehat{\widetilde{u_i}}\widehat{\widetilde{\xi}} = c_i \alpha_\xi - \widehat{c_i \beta_\xi} \tag{2-51}$$

would have to be used. The model for the sub-grid flux at the test level, α_ξ, would be of the form:

$$\alpha_\xi = \Phi_t^{1/2} (2K)^{1/2}, \tag{2-52}$$

where

$$\Phi_t = \widehat{\overline{\rho}\widetilde{\xi}\widetilde{\xi}} - \widehat{\overline{\rho}}\widehat{\widetilde{\xi}}\widehat{\widetilde{\xi}} = L_\phi + \widehat{\Phi}, \tag{2-53}$$

and

$$L_\phi = \widehat{\overline{\rho}\widetilde{\xi}\widetilde{\xi}} - \widehat{\overline{\rho}}\widehat{\widetilde{\xi}}\widehat{\widetilde{\xi}}. \tag{2-54}$$

Substituting Equations (2-50) and (2-52) into the dynamic model, (2-51), gives the following:

$$L_{u_i\xi} = c_i \Phi_t^{1/2} \left(2K\right)^{1/2} - \widehat{c_i \Phi^{1/2} \left(2k\right)^{1/2}}. \tag{2.55}$$

Equation (2.55) is a set of three Fredholm integral equations of the second kind. Although not strictly justified, the dynamic vector coefficient can be removed from the integral giving a set of three algebraic equations:

$$\tau_{u_i\xi} = \left(\frac{L_{u_i\xi}}{\Phi_t^{1/2}\left(2K\right)^{1/2} - \widetilde{\Phi^{1/2}\left(2k\right)^{1/2}}} \right) \Phi^{1/2}\left(2k\right)^{1/2}. \tag{2.56}$$

The model derived above is consistent with the dynamic structure LES model since it does not use a turbulent diffusion term to model the unclosed term. However, use of this model would require adding sub-grid transport equations for all species that are transported in the KIVA code. These sub-grid transport equations would add computation cost as well as have terms involving the mean reaction rate that would be extremely difficult to model. In order to avoid these difficulties, the sub-grid scalar flux is currently modeled using equations **(2-34)** and **(2-37)**.

Chapter 3 - Probability Density Function Time-Scale Model

3.1 Introduction

A review of combustion models in Chapter 1 showed that combustion models are either too simple to capture all the physics of the combustion process or are extremely complex and require a lot of computational effort. The PDF time-scale model presented in this study attempts to capture the major physics of the combustion process without the need for large amounts of computational effort.

Most efforts at modeling diesel combustion use a premixed combustion model and a diffusion combustion model and employ coupling between the two models. The PDF time-scale model attempts to model both these modes with a single model that can be used in all regimes of combustion. This is achieved by using a laminar flamelet concept in the flamelet regime of combustion and is modified for use in other regimes using a time-scale approach. Some of the governing equations that need to be solved to model a turbulent reacting flow are discussed followed by a discussion of the laminar flamelet concept and the time-scale modification.

3.2 Conservation Equations

In a gaseous reacting flow, mass fractions of species are governed by the equations for conservation of mass, momentum and species. The averaged form of the species conservation equation is given as (Lee, 1999):

$$\frac{\partial \overline{\rho}\widetilde{Y}}{\partial t}+\frac{\partial \overline{\rho}\widetilde{u}_i\widetilde{Y}}{\partial x_i}=-\frac{\partial \tau_{u_iY}}{\partial x_i}+\overline{\frac{\partial}{\partial x_i}D\rho\frac{\partial Y}{\partial x_i}}+\overline{\dot{\omega}}, \tag{3-1}$$

where

$$\tau_{u_iY}=\overline{\rho}\left(\widetilde{u_iY}-\widetilde{u}_i\widetilde{Y}\right). \tag{3-2}$$

The mean reaction rate term that appears in equation (3-1) is difficult to evaluate. Typically, the laminar reaction rate for an irreversible reaction such as $F+O\rightarrow P$ may be given as:

$$\dot{\omega}_P=AC_FC_O\exp\left(-\frac{E_A}{RT}\right), \tag{3-3}$$

where C represents the concentration of a species and T is the temperature. Evaluation of the mean reaction rate requires averaging the above term. Because of the way in which averages are defined, the mean reaction rate is not equal to:

$$\overline{\dot{\omega}}_P\neq-A\overline{C}_F\overline{C}_O\exp\left(-\frac{E_A}{R\overline{T}}\right). \tag{3-4}$$

Care should be taken not to use the above expression as this could result in errors up to three orders of magnitude (Jones *et al*., 1982). We make use of the laminar flamelet concept to help model the mean reaction rate since it is difficult to solve for directly.

3.3 Laminar Flamelet Concept

The laminar flamelet concept (Bilger, 1980; Peters, 1984) simplifies modeling the reaction rate term that appears in the species conservation equation. The motivation for using this concept is to simplify the turbulence-chemistry interactions by assuming a time-scale separation of turbulent and chemical time-scales in the flamelet regime. Under the laminar flamelet concept, a turbulent flame is viewed as an ensemble of laminar diffusion flamelets that are embedded in a turbulent flow field. A flamelet is a thin, locally one-dimensional, laminar structure within which reaction takes place. The strain rate scales associated with the smallest turbulent eddies are larger than those associated the flamelet and the effect of turbulence is to stretch these flamelets. Under these assumptions, the laminar flamelet solution may be mapped onto the turbulent flow field. The laminar flamelet solution can be obtained as a function of a single conserved scalar and one other parameter, which characterizes the flow field.

A conserved scalar is one that is not generated or consumed by chemical reaction. Examples of conserved scalars are the total enthalpy in adiabatic systems and elemental mass fractions. The mixture fraction, ξ, is a conserved scalar and can be defined as (Bilger, 1976):

$$\xi = \frac{Z_k - Z_{k,ox}}{Z_{k,fuel} - Z_{K,ox}} \tag{3-5}$$

Here, Z_k represents the elemental mass fraction of atomic species *k*, while *ox* and *fuel* denotes the conditions in the oxidizer and fuel boundaries, respectively. In this study, the definition of ξ is based on elemental carbon.

Under the assumption that chemical time-scales are smaller than flow time-scales, the species mass fractions are solely a function of the mixture fraction as:

$$Y_i = Y_i^e(\xi) \tag{3-6}$$

This argument of chemical time-scales being smaller than flow time-scales leads to an equilibrium assumption. Species mass fractions as a function of the mixture fraction under the equilibrium assumption are show in figure 3-1:

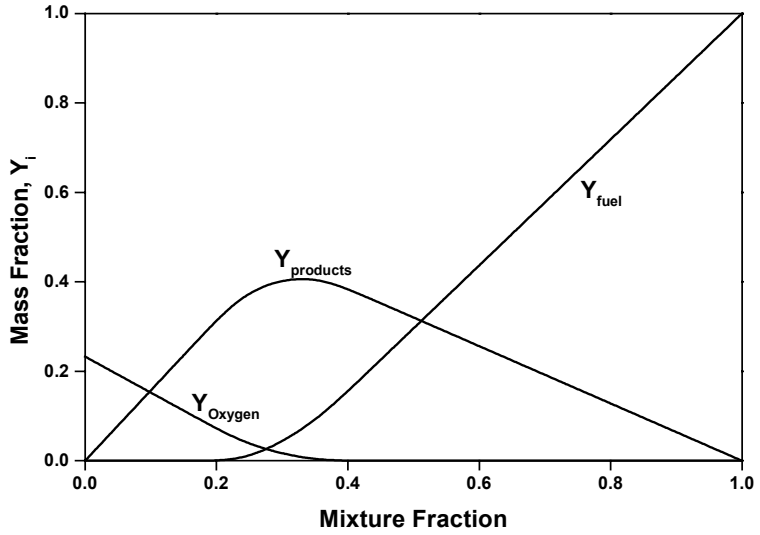

Figure 3-1: Species Mass fractions as a function of mixture fraction for the equilibrium assumption

Implied in the equilibrium assumption is that the mixture fraction is uniform throughout the flow field, i.e. no gradients in mixture fraction are present. However, this is often not the case in non-premixed combustion and the solution obtained in equation (3-6) does not consider the effect of gradients. The parameter that is used to account for these gradients is the stretch rate, χ, which is defined as

$$\chi = 2D\frac{\partial \xi}{\partial x_k}\frac{\partial \xi}{\partial x_k} \tag{3-7}$$

Under the laminar flamelet concept, it is assumed that the reaction zone is a thin region around the surface of the stoichiometric mixture fraction. If a new co-ordinate system is attached to this surface, the mixture fraction becomes a new co-ordinate, which is locally normal to the stoichiometric surface. The species conservation equation may be transformed into this new co-ordinate system where the mixture fraction is the independent variable. The transformation results in the flamelet equation for species conservation (Peters, 1984):

$$\rho \frac{\partial Y_i}{\partial \tau} - \rho \frac{\chi}{2Le_i} \frac{\partial^2 Y_i}{\partial \xi^2} - \dot{\omega}_i = 0 , \tag{3-8}$$

where τ is time in the new-coordinate system.

The flamelet equations in mixture fraction space do not have any convective terms and the stretch rate, χ, accounts for both convection and diffusion normal to the surface of stoichiometric mixture fraction. The stretch rate may also be viewed as an external parameter that is imposed on the flamelet due to the flow field (Peters, 1984). Using the laminar flamelet concept, the species mass fractions may be expressed as:

$$Y_i = Y_i(\xi, \chi) \tag{3-9}$$

Equation (3-9) assumes that the Damköhler number is large (chemical time-scales are much smaller than flow time-scales). However, there are some regimes in Diesel Combustion where the Damköhler number is not large (Peters – length scales paper). These regimes are illustrated in figure 3-2.

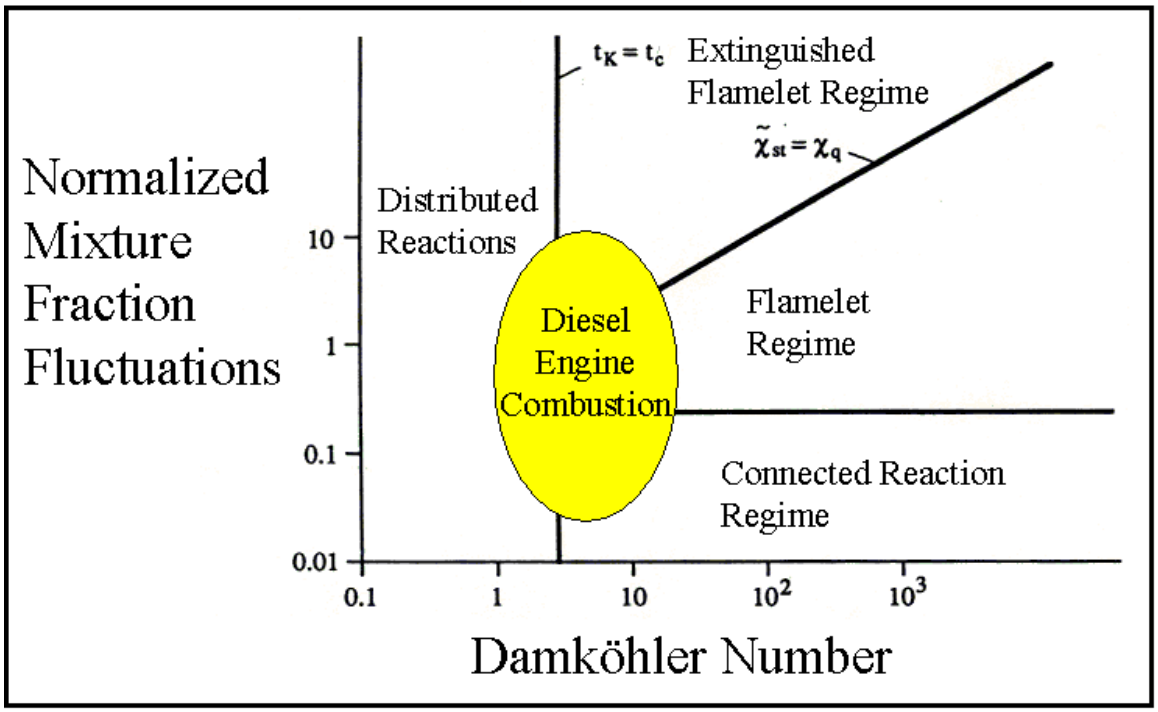

Figure 3-2: Regimes of Diesel Combustion

In order to use the flamelet combustion model in these regimes, it must be modified to take into account that chemical and turbulent time-scales may be of the same order of magnitude. The modifications used in this study are discussed in section 3.4.

3.3.1 Opposed Flow Diffusion Flame

It is believed that a good representation of a stretched laminar flamelet is the opposed flow diffusion flame. This configuration has been studied extensively by a number of researchers (reference) because it is simple enough for detailed experimentation to be performed, yet complex enough for studying phenomena such as strain and detailed kinetics.

A schematic of the configuration is shown in figure 3-3 (Lee, 1999). The arrangement consists of jets of pure fuel and oxidizer that diffuse into each other. A diffusion flame is formed at the point where the fuel and oxidizer meet in stoichiometric proportion. In this study, the OPPDIF code (Lutz *et al*., 1997) was used to solve the equations governing an opposed flow diffusion flame. The program requires a chemical mechanism as an input parameter. For the engine simulations that are discussed in Chapter 4, an iso-octane mechanism consisting of 29 species and 49 reactions was used (reference). For the reacting jet simulation, a chemical mechanism for methane-air combustion with 37 species and 190 reactions (reference) was used. For the engine simulations, the OPPDIF calculations were performed at 100 atm. pressure and the fuel and oxidizer inlet temperatures were assumed as 300 K and 1000 K respectively. For the reacting jet simulation, the pressure was set to 1 atm and fuel and oxidizer inlet temperatures were set to 300 K when performing OPPDIF calculations.

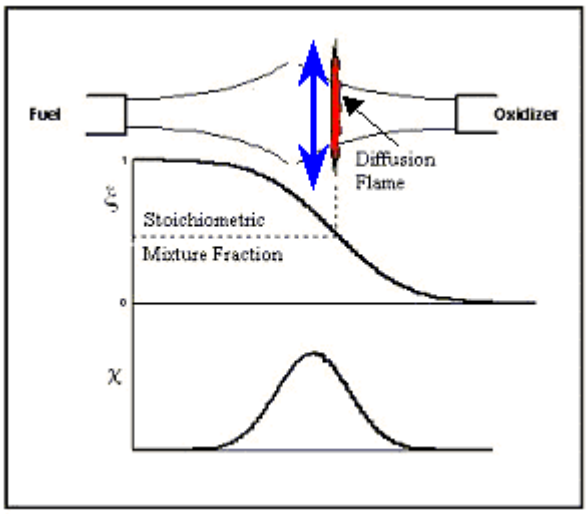

Figure 3-3: Opposed flow diffusion flame configuration

For the simple case of the opposed flow diffusion flame, the mixture fraction varies from one at the fuel inlet to zero at the oxidizer inlet boundary. The point of stoichiometric mixture fraction is shown in figure 3-3. The thin region around the vicinity of this stoichiometric mixture fraction is known as a laminar diffusion flamelet. The mixture fraction can be made the independent variable in the opposed flow diffusion flame solution and this solution is assumed to be the solution to equation (3-8).

The stretch rate, χ, is varied in this configuration by varying the fuel and oxidizer boundary velocity. As χ gets larger, the rate at which fuel and oxidizer are transported into the reaction zone is increased. As χ approaches zero, the laminar opposed flame solution approaches the equilibrium solution shown in figure 3-1.

The effects introduced by the stretch rate are important. Although the reaction rate increases as χ increases, the temperature decreases with increasing χ. This effect can be seen in figure 3-4, which shows the temperature and fuel reaction rate as a function of the mixture fraction for different values of the stretch rate. This apparent contradiction of the temperature decreasing while the reaction rate increases is due to the stretching of the laminar flamelet with the increase in stretch rate. As the laminar flamelet is stretched, its thickness in physical space decreases. Due to this, heat conduction from within the reaction zone increases, causing the temperature to drop. In other words, the rate of increase of reaction rate is not sufficient to keep up with the increased rate of heat loss due to thinning of the flamelet. This effect continues until the stretch rate reaches a critical value known as the quenching value of the stretch rate where the kinetics cannot

keep up with the rate at which the fuel and oxidizer are transported into the reaction zone and the flamelet is quenched.

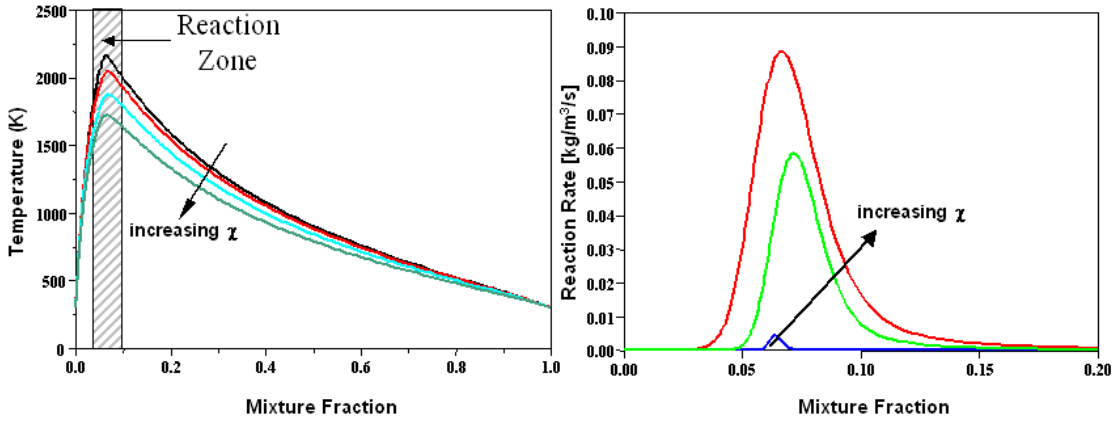

Figure 3-4: Effect of Stretch Rate on Temperature and Reaction Rate

For the iso-octane mechanism used in this study, the quenching value of χ was found to be 142.2 s^{-1} at the conditions the OPPDIF simulations were performed. For the methane – air mechanism, the quenching value of χ was found to be 16.0014 /s which is in agreement with experimental findings (reference from Peter's reduced mechanisms book).

3.3.2 Extension to Turbulent Flow Simulation

Using the opposed flow configuration, we can obtain all scalars of interest (such as temperature and mass fractions) as a function of the mixture fraction and the stretch rate. When performing a turbulent flow simulation, we need average values of the scalars because these are solved for with conservation equations. Moreover, the instantaneous mixture fraction and stretch rate cannot be determined because of computational

limitations. Instead, the statistics for these quantities can be determined by solving transport equations, and the mean values of the scalars of interest can then be determined knowing the statistics of the mixture fraction and the stretch rate. The mean mixture fraction may be obtained by solving equation **(2-32)**. Similarly, the second moment of the mixture fraction is obtained by solving equation **(2-38)**. The term, χ, that appears in equation **(2-38)** is the rate of dissipation of sub-grid mixture fraction fluctuations and is useful in determining the mean stretch rate. Once the mean mixture fraction, its second moment, and the mean stretch rate are know, they can be used to determine mean values of the scalars from the instantaneous OPPDIF solutions using Probability Density Functions as explained below.

3.3.3 Probability Density Function

A probability density function (PDF) describes the likelihood that a continuous random function, f, lies in an interval between $f+\Delta f$ and $f-\Delta f$. An important property of the PDF is that the integral of the PDF over all possible values of the function must equal one:

$$\int_{-\infty}^{+\infty} P(f)df = 1 \tag{3-10}$$

where $P(f)$ is the probability density function of the variable f.

Once the PDF of a variable f is known, the mean value of any variable, $\alpha = \alpha(f)$, can be found using the following expression:

$$\overline{\alpha} = \int_{-\infty}^{+\infty} \alpha(f) P(f) df \tag{3-11}$$

Using this method, mean scalar values can be determined from instantaneous OPPDIF simulations.

For a PDF to perfectly describe a continuous random variable, an infinite number of moments are required to be known. However, due to computational limitations, it is assumed that the PDF of the mixture fraction may be found knowing it's first two moments and the PDF of the stretch rate may be found knowing it's first moment. Knowing these moments, a distribution is assumed for the shape of the PDF of the mixture fraction and the stretch rate. This method of constructing a PDF using an assumed shape characterized by the moments of the variable is known as the presumed probability density function (PPDF) method of combustion modeling. In this study, it is assumed that the PDF of the mixture fraction is a beta-distribution given as:

$$P(\xi) = \frac{\xi^{\alpha-1}(1-\xi)^{\beta-1}}{\int_0^1 \xi^{\alpha-1}(1-\xi)^{\beta-1} d\xi} \tag{3-12}$$

where

$$\alpha = \widetilde{\xi}\left[\frac{\widetilde{\xi}(1-\widetilde{\xi})}{\widetilde{\xi''^2}} - 1\right], \tag{3-13}$$

and

$$\beta = (1-\widetilde{\xi})\left[\frac{\widetilde{\xi}(1-\widetilde{\xi})}{\widetilde{\xi''^2}} - 1\right]. \tag{3-14}$$

The PDF of the stretch rate is assumed a lognormal distribution (Lee, 1999) given as:

$$P(\chi) = \frac{1}{\chi\sigma_\chi\sqrt{2\pi}} \exp\left(-\frac{\left(\ln(\chi) - \overline{\chi}\right)}{2\sigma_\chi^{\,2}}\right) \tag{3-15}$$

where $\overline{\chi}$ is the mean stretch rate, which is determined using methods discussed in section 2-4 and σ_χ is the standard deviation, which is assumed unity. It has been shown that mean properties of interest are relatively insensitive to the precise shape of the PDF (Jones et al., 1982).

Having determined the PDFs of the mixture fraction and the stretch rate, the mean mass fractions are determined from the instantaneous OPPDIF solutions as:

$$\tilde{Y}_i = \int_0^\infty \int_0^\infty Y_i(\chi,\xi) P(\chi,\xi) d\xi d\chi \tag{3-16}$$

It is assumed that the stretch rate and the mixture are statistically independent which simplifies the evaluation of equation (3-16):

$$\tilde{Y}_i = \int_0^{\chi_q} \int_0^1 Y_i(\chi,\xi) P(\chi) P(\xi) d\chi d\xi \tag{3-17}$$

Mass fractions determined using equation (3-17) are tabulated as a function of the mean mixture fraction, its second moment and the mean stretch rate. Pre-computing the integral in equation (3-17) and tabulating the mass fractions offers a computational advantage, as the integral need not be evaluated during the simulation. However, with this advantage comes a penalty in accuracy, as interpolation is necessary to determine mean mass fractions. In order to improve the accuracy of this interpolation, high resolution in storing tabulated values was used around the stoichiometric mixture fraction where large gradients in mass fractions exist.

It has been shown (Lee, 1999) that choosing 13 of the 29 species from the original mechanism used in the OPPDIF simulations account for over 99% of the mass. To avoid

the computational expense of transport equations for all the species, it was decided to transport only these 13 species. The KIVA code was modified to allow for transport of six additional species, i.e. $C_2H_2, CH_3, C_2H_4, C_3H_4, C_3H_6$, and C_4H_8, apart from the seven species for which KIVA already solved transport equations.

3.4 Time-scale approach for Low Damköhler Number Effects

As noted in section 3.3, the laminar flamelet model needs to be modified for use in regions of low Damköhler number. In order to model combustion in these regimes, a modified form of the characteristic time-scale model of Reitz *et al.* (1983) is used. This method is discussed here. Equation (3-8) may be written as:

$$\frac{\partial Y_i}{\partial t} = \frac{\chi}{2Le_i}\frac{\partial^2 Y_i}{\partial \xi^2} + \frac{\dot{\omega}_i}{\rho} \tag{3-18}$$

In the PDF time-scale model, the right hand side of equation (3-18) is expanded to first order in time about the flamelet solution using a Taylor series expansion resulting in:

$$\frac{\partial Y_i}{\partial t} = \left(\frac{\chi}{2Le_i}\frac{\partial^2 Y_i}{\partial \xi^2} + \frac{\dot{\omega}_i}{\rho} \right)^* + \sum_{j=1}^{n} \alpha_{ij} \left(Y_j - Y_j^* \right) \tag{3-19}$$

where J is the number of species and * indicates the steady OPPDIF solution. The leading order term $\left(\frac{\chi}{2Le_i}\frac{\partial^2 Y_i}{\partial \xi^2} + \frac{\dot{\omega}_i}{\rho} \right)^*$ must equal zero since the OPPDIF solution is a steady solution. The Jacobian matrix α_{ij} contains the elements $\frac{\partial \left(\frac{\chi}{2Le_i}\frac{\partial^2 Y_i}{\partial \xi^2} + \frac{\dot{\omega}_i}{\rho} \right)^*}{\partial Y_j}$ evaluated for the steady flamelet solution. Note that the elements of α_{ij} are reciprocal time-scales of species Y_j with respect to terms in flamelet equation i. This matrix can be

evaluated numerically from the steady OPPDIF solution. A representative term, τ_{CO_2}, for one OPPDIF simulation is shown in figure 3-5.

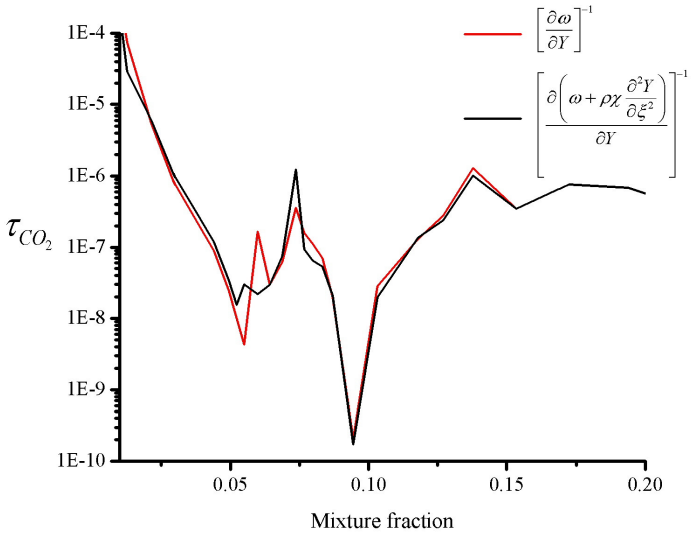

Figure 3-5: Representative time-scale for PDF time-scale model

The original characteristic time-scale model of Reitz *et al*. expands the reaction rate term about equilibrium and turbulence effects are introduced by modifying the time-scale as a combination of a laminar and a turbulent time-scale. The difference between expanding the reaction rate term and the $\frac{\chi}{2Le_i}\frac{\partial^2 Y_i}{\partial\xi^2}+\frac{\dot{\omega}_i}{\rho}$ term can be seen in figure 3-5.

It is currently assumed that all off-diagonal terms of α_{ij} are zero and all diagonal terms can be represented by a time-scale $1/\tau_{chem}$:

$$\tau_{chem} = A^{-1}\left(Y_{fuel}\right)^{0.75}\left(Y_{O_2}\right)^{-1.5}\exp\left(\frac{E_A}{RT}\right) \tag{3-20}$$

where $A = 1.54e+10$ and $E_A = 77.3\ kJ/mol$. These values are determined from a one-step reaction-rate expression for tetradecane (Kong et al., 1995).

With this method, the time rate of change of species i is then written as:

$$\frac{\partial \tilde{Y}_i}{\partial t} = -\frac{\tilde{Y}_i - \tilde{Y}_i^*}{\tilde{\tau}_{chem}} \tag{3-21}$$

where $\tilde{Y}_i^*$ is the value of the mass fraction obtained from equation (3-17). Equation (3-21) is integrated in time to yield an expression for the mean mass fraction of species i at time $n+1$:

$$\tilde{Y}^{n+1} = \tilde{Y}_i^* + (\tilde{Y}_i^n - \tilde{Y}_i^*)e^{(-\Delta t/\tau_{chem})} \tag{3-22}$$

The second term in equation (3-22) can be thought of as a perturbation added to the steady flamelet solution to account for low Damköhler number effects. It can be seen that as τ_{chem} becomes very small (large Damköhler number), the mean mass fractions obtained from the steady flamelet solution are recovered.

Future work will consider multiple time-scales since each species reacts at a different rate. This will involve determining all elements of the Jacobian Matrix α_{ij} from the OPPDIF solution. In addition, the characteristic time-scale for combustion can be obtained by weighting $\dfrac{\partial\left(\dfrac{\chi}{2Le_i}\dfrac{\partial^2 Y_i}{\partial \xi^2} + \dot{\omega}_i\right)}{\partial Y_j}$ with the Joint PDF of the mixture fraction and the stretch rate.

Chapter 4 - Turbulent Combustion Simulations using the PDF time-scale model

A predictive combustion model should be able to predict combustion in both simple and complex flows over a wide range of flow conditions. To test the models developed in this study, it was decided to apply the models to simulate a reacting methane-air jet flame as well as for simulations of various internal combustion engines. Results and discussions based on these simulations are presented in this chapter.

4.1 Reacting Jet Simulation

It is believed that in order to test the combustion model, it should be applied to a simple reacting flow where complex physics like sprays, two-phase flow and evaporation are not present. With this objective, the PDF time-scale model was used to simulate the reacting methane-air jet flame studied experimentally by Barlow *et al.* (1998a, 1998b). The Dynamic Structure LES model (Section 2.3.3) was used to model turbulence. This flame is sometimes referred to as the Sandia flame D.

The experimental setup consists of a main fuel jet of diameter 7.2 mm. The main jet composition is 25% methane and 75% air. The main jet is surrounded by a burnt-gas pilot of diameter 18 mm. The pilot is a lean (phi=0.77) pre-mixture of C_2H_2, H_2, air, CO_2, and N_2 with the same nominal enthalpy and equilibrium composition as methane/air at this equivalence ratio. The energy release of the pilot is approximately 6% of the main jet and the temperature of the burnt gases is approximately 1880 K. The pilot stream is

surrounded by an air co-flow. The Reynolds number based on the fuel stream is 22400. The mixing rates in these flames are high enough that these flames burn as diffusion flames, with a single reaction zone near the stoichiometric mixture fraction and no evidence of premixed reaction in the fuel-rich CH_4/air mixtures is found.

The computations were performed using a 3-d Cartesian mesh. The dimensions of the mesh are 30 cm x 30 cm x 60 cm and the mesh has approximately 280,000 cells. A Cartesian mesh was chosen for the simulation because some LES filtering properties used in developing the LES equations are not valid for cylindrical cells. A view of this mesh is shown in figure 4-1. The cells get larger in all three co-ordinate directions away from the jet inlet for computational efficiency.

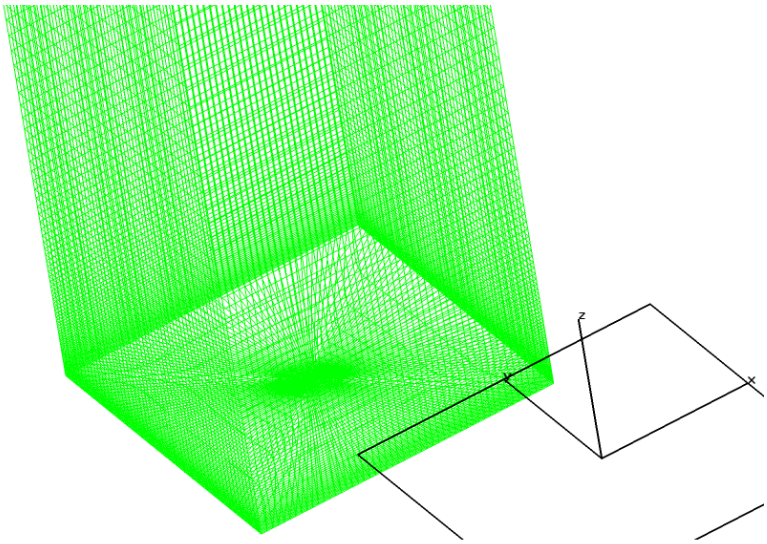

Figure 4-1: Cartesian Mesh used for simulation of Sandia Flame D

Boundary conditions for the velocity and scalars were obtained from experimental data and the KIVA code was modified to impose these boundary conditions. The sub-grid kinetic energy, k (see section 2.3.3), was perturbed in time to represent turbulent fluctuations in the velocity.

The simulation was first run for approximately 1.5 flow-through times (~0.075 s). The simulation was then restarted and ensemble averages of quantities of interest were computed every 100 time-steps (approximately every 0.001 s). The averages reported here are taken at 0.16 s.

Figure 4-2 shows an instantaneous snapshot of the LES mean temperature and LES mean stretch rate at 0.08 s. The mean temperature is shown in a plane passing through the center of the main jet. Tthe whole domain in the length-wise direction is shown. The mean stretch rate is shown in the same plane and is magnified to show the jet inlet region. The black line corresponds to a contour of the stoichiometric mean mixture fraction. The presence of large-scale structure is evident in both the temperature and stretch rate images. It is expected that such structure would not be seen in a RANS simulation.

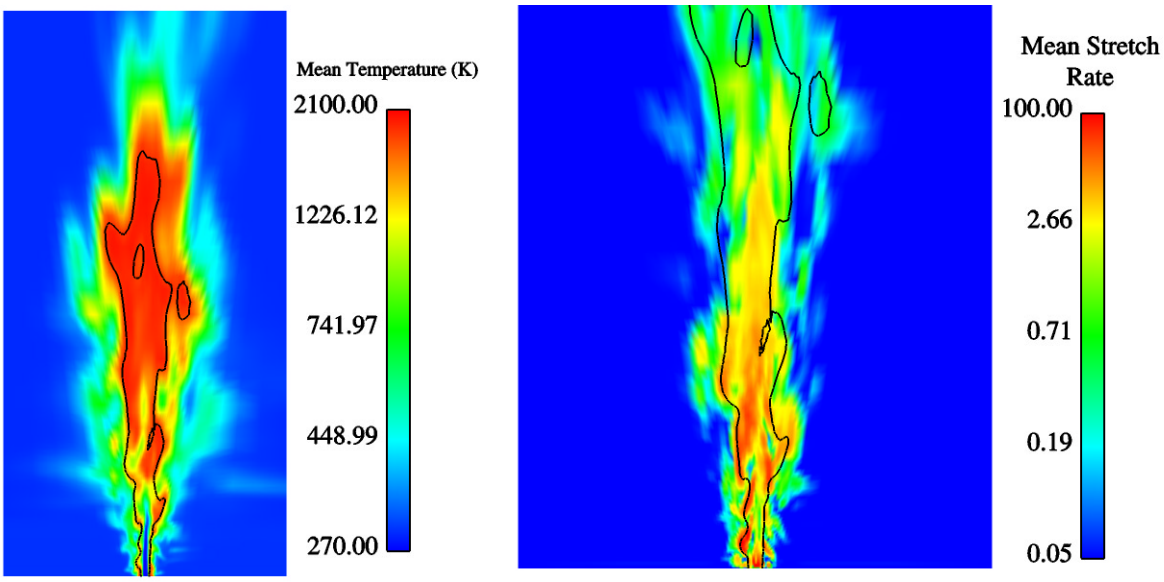

Figure 4-2: Instantaneous temperature and stretch rate for the Sandia Flame D simulation

The peak temperatures in the upstream region of the jet are around the stoichiometric fraction indicating that reaction takes place around that region. This agrees with the experimental findings of Barlow *et al*. In the downstream region, high temperatures are seen both around the stoichiometric mixture fraction and in regions surrounding it.

The LES simulation of the jet shows large stretch rates in the reaction zone (around regions of stoichiometric mixture fraction). This result agrees well with simulations of opposed flow diffusion flames (figure 3-3). It is important to predict the stretch rate correctly in order to correctly predict phenomena such as local extinction and RANS models do not do a very good job of predicting the stretch rate (Peters et al., 1988). This is believed to be a significant advantage of using the Dynamic Structure LES model in turbulent combustion simulations.

Radial values of the ensemble-averaged temperature predicted by the model are compared with experimental values in figure 4-3. The model results have been averaged in the θ- direction. Radial profiles at 1, 2, 15, and 45 diameters downstream of the jet exit are shown.

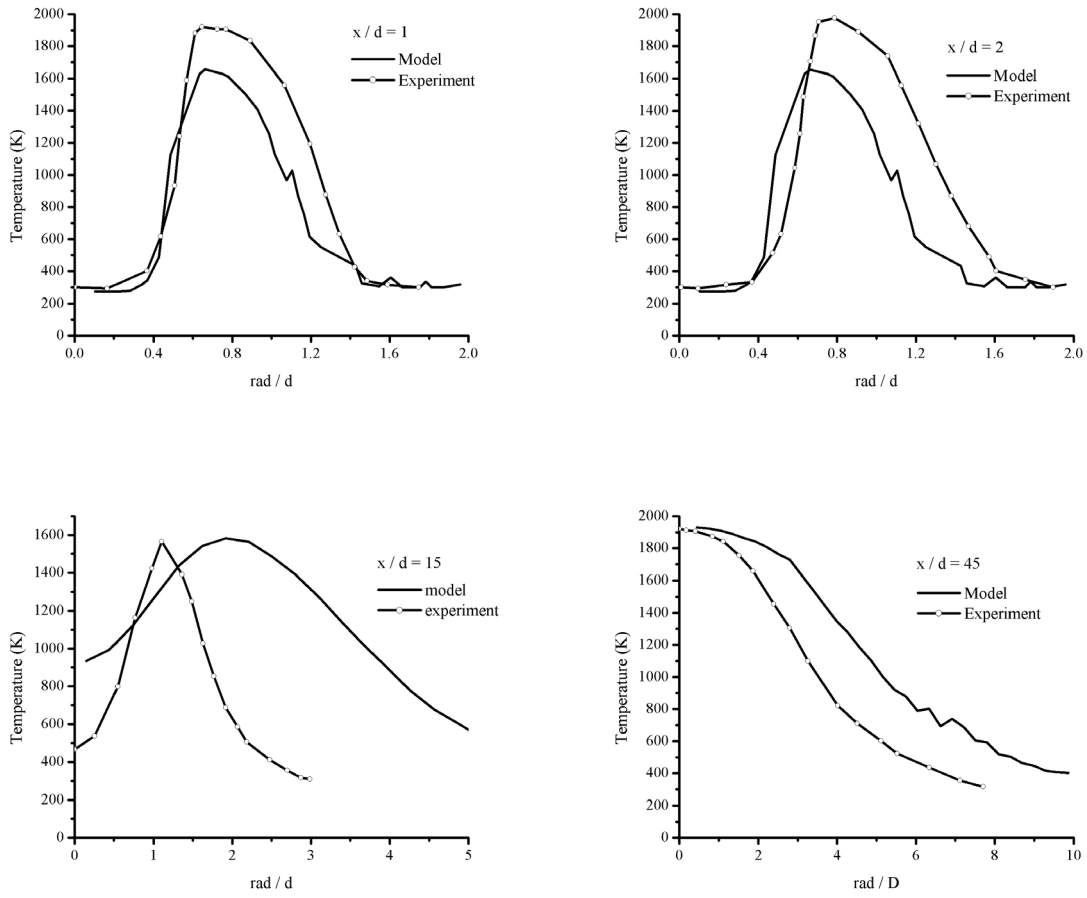

Figure 4-3: Radial Profiles of temperature for four locations in the axial direction for a simulation of Sandia Flame D

The shape of the temperature profiles at each location agrees with the experiment. For the two upstream positions, the magnitude of the peak temperature is under-predicted by

the model indicating that predicted combustion in these regions is not as pronounced as in the experiment. One possible reason for this is that the high stretch rates in this region cause local quenching of the flame. The manner in which spatial derivates are calculated in the KIVA code leads to high stretch rates near the inlet. This result indicates that the model for predicting local quenching must be improved and the calculation of derivates near boundaries needs to be modified.

In the two downstream regions, the peak temperatures are in reasonable agreement with the experiment; however, the location of peak temperature is incorrect. It appears that the spread-rate of the jet is higher for the simulation than the experiment. Two possible reasons for this are absence of buoyancy effects in the simulation and the magnitude of the perturbation on the inlet sub-grid kinetic energy, which may be resulting in more turbulence than what is observed experimentally.

4.2 Engine Simulations

Having verified that the combustion model can predict combustion in simple flows satisfactorily, it was decided to test the models for simulating Diesel Combustion in different engines at various load conditions to test the predictive ability of the model in more complex flows. The test engines used in this study are a single Cylinder version of the Caterpillar 3400 series engine (Montgomery *et al*, 1996) (referred to as the old Caterpillar engine), a new single cylinder version of the Caterpillar 3401 engine (need reference) (referred to as the new Caterpillar engine), and an optical access engine (Dec, 1997) (referred to as the Sandia Optical access engine). The old caterpillar engine is

operated under a baseline operating mode and a 6-mode test cycle. The Sandia engine is operated under one operating condition and the new Caterpillar 3401 engine was tested for two different modes. The various operating conditions for the old Caterpillar and the Sandia engines are shown in the table 4-1.

Engine and Operating Mode	Speed (rpm)	% Load	θ_{INJ} (CA° ATDC)	$\dot{m}_{fuel}$	P_{in} (kPa)
Caterpillar 3400 (Baseline)	1600	75	-9.0	129 g/min	183
Caterpillar 3400 (Mode 1)	750	0	-8.0	8.7 g/min	100
Caterpillar 3400 (Mode 2)	953	25	-0.5	33.7 g/min	108
Caterpillar 3400 (Mode 3)	1074	75	5.5	105.0 g/min	168
Caterpillar 3400 (Mode 4)	1657	100	7.5	169.0 g/min	239
Caterpillar 3400 (Mode 5)	1668	50	2.0	88.8 g/min	164
Caterpillar 3400 (Mode 6)	1690	25	-1.0	53.8 g/min	132
Sandia	1200		-11.5	0.0535 g/cycle	206

Table 4-1: Operating conditions for the old Caterpillar and Sandia engines

For the majority of the simulations, a sector mesh was used for computational efficiency. The Caterpillar mesh is a 60° sector while the Sandia mesh is a 45° sector (verify), as seen in figure 4-4.

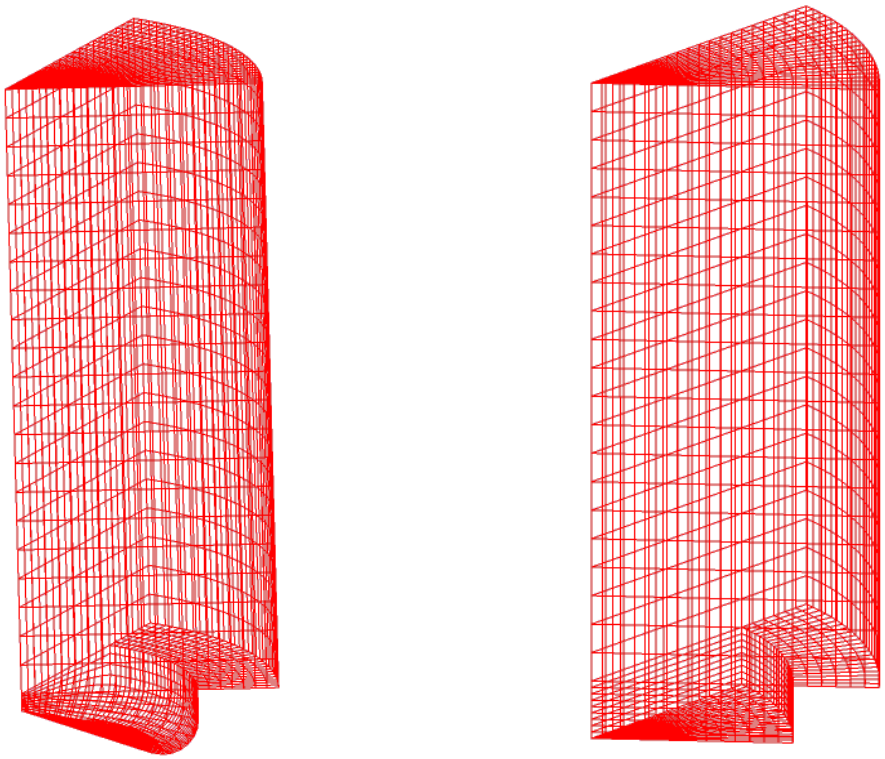

Figure 4-4: Perspective view of the computational mesh for the Caterpillar 3401 engine (left) and the Sandia Optical access engine (right)

The simulations for the new Caterpillar engine were done using a 360° Cartesian mesh. These cases are discussed further in section 4.2.2.3.

The remainder of this chapter is organized as follows. Results from simulations using the PDF time-scale model using the RNG $k-\varepsilon$ model (reference) for turbulence are first presented. This is followed by results from simulations using the Smagorinsky model (section 2.3.1) and the one-equation viscosity model (section 2.3.2) for turbulence. Finally, results using the dynamic structure model (section 2.3.3) with the PDF time-scale model are presented.

All the simulations used the UW – ERC modified version of the KIVA-3V code with the PDF time-scale combustion model. Standard ERC sub-models (Han *et al*., 1994) were used. Ignition was simulated using the shell ignition model (reference). Most constants used in the ERC sub-models were left unchanged. The constants that were changed and their values are shown in table 4-2. All simulations were started at intake valve closure and run until end of combustion.

Constant	Value
denomc: pre-exponential coefficient in timescale τ_{chem}	0.3e10
tchop: Temperature at which switch is made from shell model to combustion model	1100 K
af04: pre-exponential coefficient for reaction 4 in Shell Ignition Model	1.5e5

Table 4-2: Constants used for ERC sub-models

For all the engine simulations using LES, the turbulent law-of-the-wall model was turned off and walls were set to a no-slip boundary condition. Since the law-of-the-wall relies on quantities such as k and ε from RANS models, it was decided not to use this model. Developing wall models for LES is an area that needs future research.

4.2.1 Engine Simulations with the PDF time-scale model and RANS turbulence models

The first test of the PDF time-scale model as a predictive combustion model for I.C. engine simulations was to simulate various operating conditions for two test engines.

Figure 4-5 shows the cylinder pressure and the heat release as a function of crank angle for the baseline operating condition of the old Caterpillar engine (table 4-1)

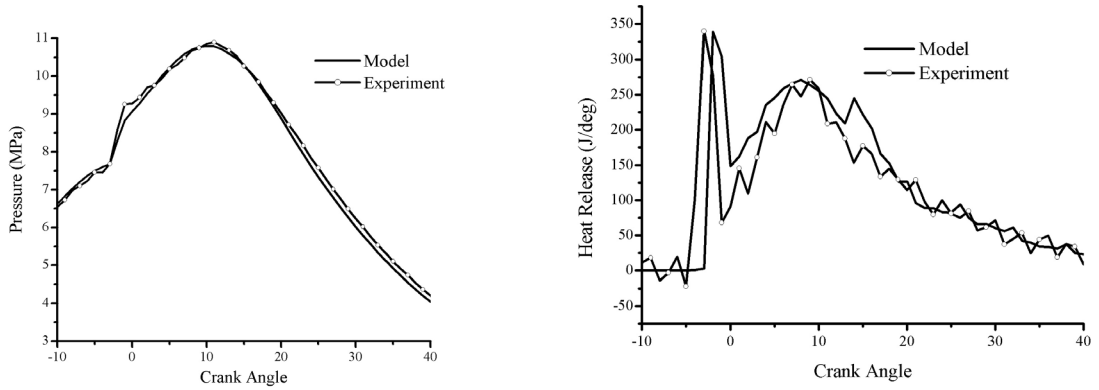

Figure 4-5: Comparison of simulated and measured pressure and heat release for the old Caterpillar engine operating at the baseline condition

It can be seen that the model matches the experimental pressure trace and the heat release curves very closely. The major features of combustion such as the premixed burn and peak pressure are captured accurately. The start of combustion is slightly delayed in the model as compared to the experiment and this may account for the slight difference in the rate of initial pressure rise around -3° ATDC as seen in the cylinder pressure plot. This may in part be due to the ignition phenomenon not being accurately captured by the Shell model. This could be changed by changing the pre-exponential constant, *Af04*, in the Shell model. However, this may require case-by-case tuning, so this constant was kept at one value for all simulations.

To further test the predictive capability of the model, the Sandia Optical access engine was simulated and results from that simulation are shown in figure 4-6.

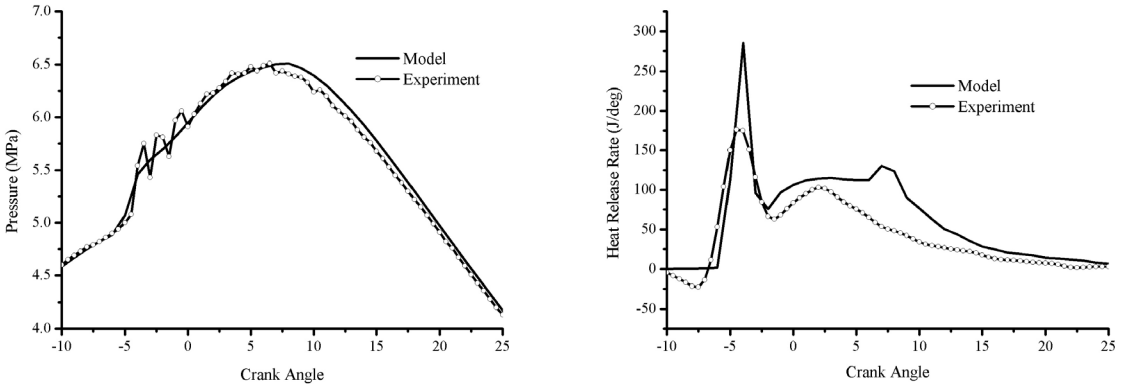

Figure 4-6: Comparison of simulated and measured pressure and heat release for the Sandia Optical Access engine.

In this simulation too, the major features of the combustion process are captured accurately. These include the premix burn, the phasing of the pressure rise, and the peak pressure. Although the heat release in the premixed burn seems to be over-predicted, the pressure rise due to the premixed burn is in agreement with experimental results. In this simulation also, the start of combustion seems to be delayed which again indicates the need to change constants in the shell model.

The six-mode test cycle for the old Caterpillar engine was simulated next. This test cycle has been previously simulated in a study by Xin *et al*. (1997). It was shown in this case that the one of the shell model pre-exponential coefficients, *af04*, had to be changed to match the ignition for each mode. In this study, that constant was left unchanged for each mode. Cylinder pressure as predicted by the model is compared with experimental values in figure 4-7.

Overall, the combustion model captures the trend in the pressure rise for all modes accurately. Some of the details are not captured accurately such as the peak pressure in modes 2 and 5. It is also observed that the ignition delay is not captured accurately for some of the cases and this could possibly have affected results from the combustion model. In addition, more work is needed in making the mixture fraction fully consistent with cases where EGR is present and this is an area of future research.

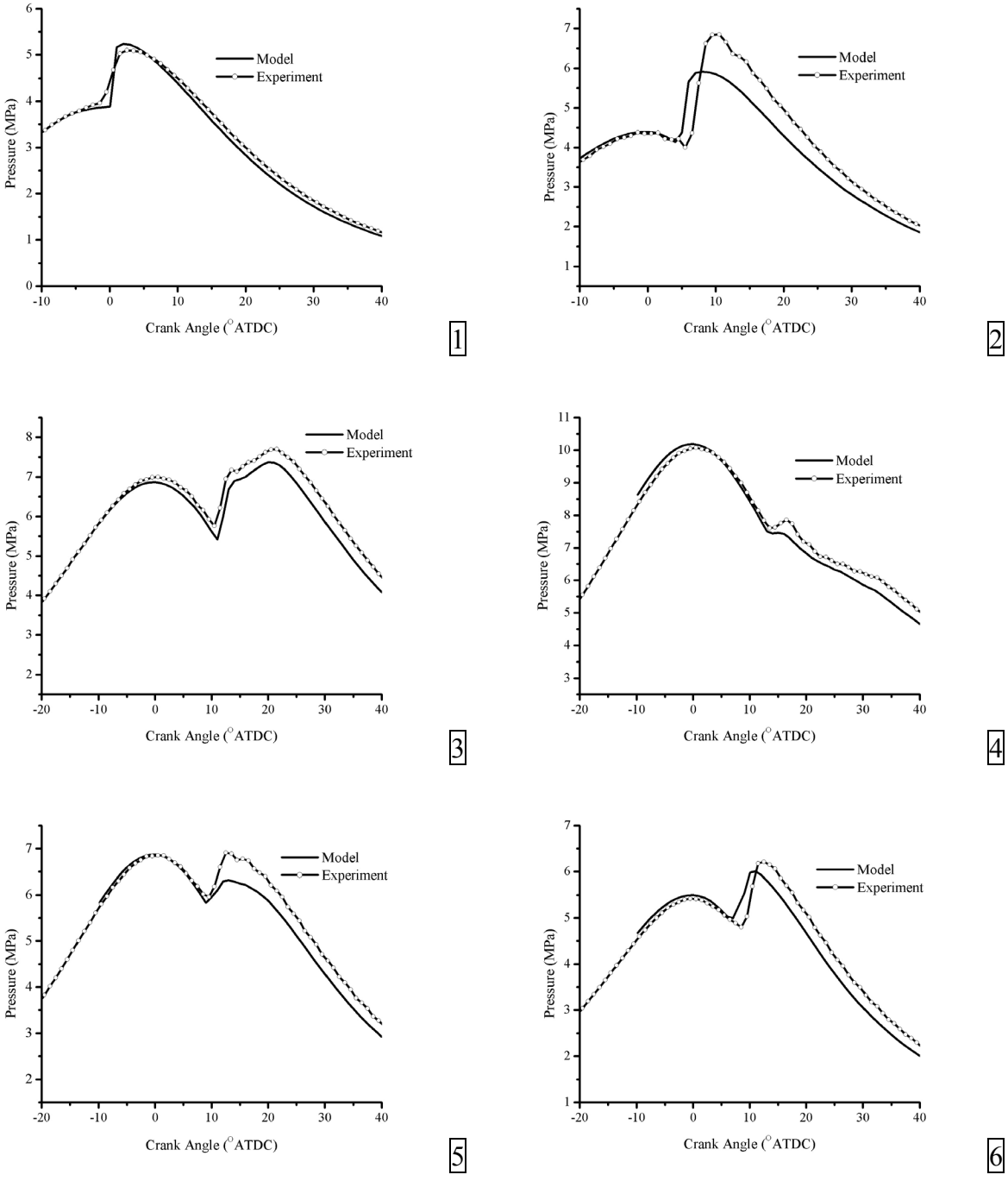

Figure 4-7: Model predicted pressures as compared to experimental values for the six-mode test cycle for the old Caterpillar 3401 engine (Numbers at bottom right of figure indicate mode number)

4.2.2 Engine Simulation using LES turbulence models

Having verified that the PDF time-scale model is able to predict major trends in the Diesel combustion process, it was integrated with LES methods of modeling turbulence. For reasons discussed earlier, it is believed that LES methods may be better suited for IC engine simulations than RANS methods.

The LES equations typically require a length scale, Δ (see for example section 2.3.1). For a uniform mesh, this length scale is usually taken as the cube root of the cell volume. However, some of the engine simulations in this study used a cylindrical mesh where cells near the axis are much smaller than those far from the axis. To avoid any difficulties that may arise from non-uniform cells, a representative length scale was used. This length scale was set to cube root of the total volume of the mesh divided by the number of computational cells when the piston is at bottom dead center.

4.2.2.1 Smagorinsky LES model

The first model implemented into the KIVA code was the Smagorinsky model discussed in section 2.3.1. The old Caterpillar engine baseline case and the Sandia Optical engine (table 4-1) were simulated using the PDF time-scale model with the Smagorinsky model.

Results from engine simulation the old Caterpillar engine are shown in figure 4-8. The pressure and heat release are in reasonable agreement with the experimentally measured values. Note that the differences could be compensated for by adjusting some of the

constants in the combustion model. However, this was not attempted, in part due to the limitations of the Smagorinsky model.

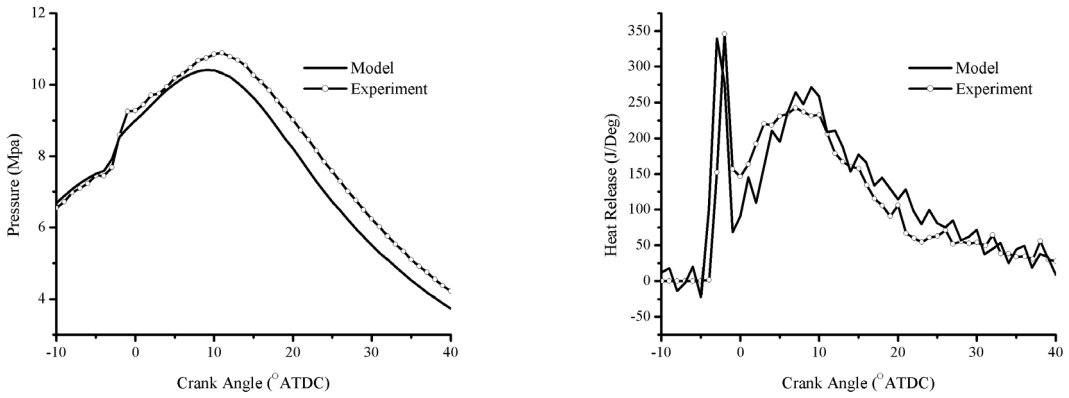

Figure 4-8: Simulated and measured pressure (left) and heat release (right) for the old Caterpillar engine using the PDF time-scale model with a Smagorinsky LES model

Results from a Sandia engine simulation for the same model are shown in figure 4-9.

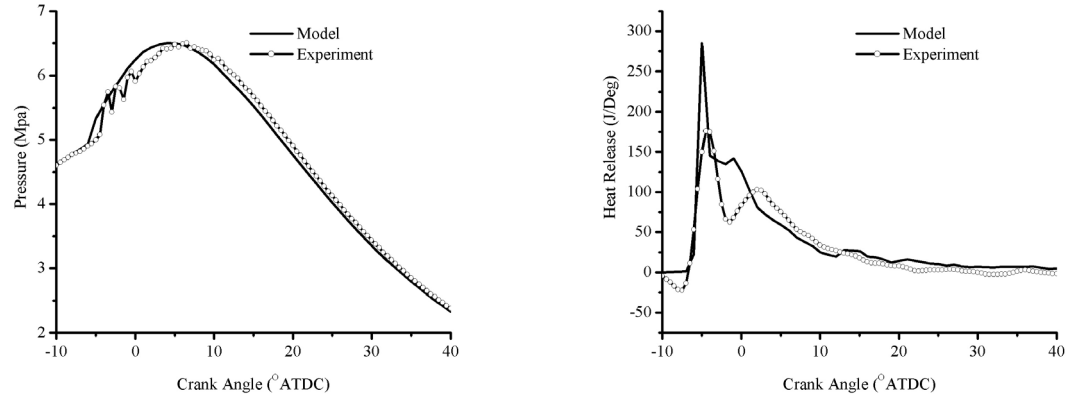

Figure 4-9: Results from simulation of the Sandia engine using the PDF time-scale model with a Smagorinsky LES turbulence model.

The predicted pressure and heat release are in reasonable agreement with the experimental results. These cylinder-averaged quantities are not very different from simulations using the RANS turbulence model. It would be expected that in-cylinder contour of quantities such as temperature, etc. would however differ from a simulation using a RANS model. However, due to the coarse grid used, the viscosity added by using the Smagorinsky model tends to smear out structures, so little difference was noted.

It is useful to examine the effect introduced by the time-scale in the PDF time-scale model. This effect is seen in figure 4-10 by looking at the multiplicative factor on the perturbation term in equation **(3-22)**, $\exp\left(-\frac{\Delta t}{\tau_{chem}}\right)$, as a function of the crank angle. The heat release as a function of crank angle is also plotted in the same figure. It is seen that the multiplicative factor approaches one at the beginning of combustion, indicating that the magnitude of the perturbation term is large at the beginning of combustion indicating a low Damköhler number at that time. This corresponds with the sharp heat release rate or the premixed burn phase where reactions are kinetically limited. The term then approaches zero as combustion proceeds and the steady flamelet solution is approached indicating that reactions are mixing limited (high Damköhler number). This finding is consistent with the physical description of the diesel combustion process provided in Chapter 1.

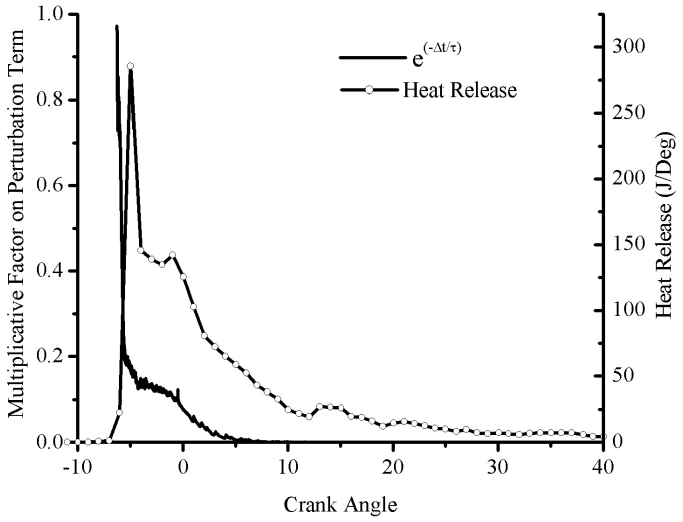

Figure 4-10: Magnitude of perturbation term and Heat Release as a function of crank angle for the Sandia Engine simulated using the PDF time-scale model with a Smagorinsky turbulence model

4.2.2.2 One-equation viscosity LES turbulence model

A one-equation viscosity based LES turbulence model was implemented into the KIVA code (see section 2.3.2). Engine simulations using this model with the PDF time-scale model were performed for the baseline operating condition of the old Caterpillar engine and the Sandia engine. Plots of cylinder pressure and heat release as a function of crank angle are compared to experimental values in figure 4-11.

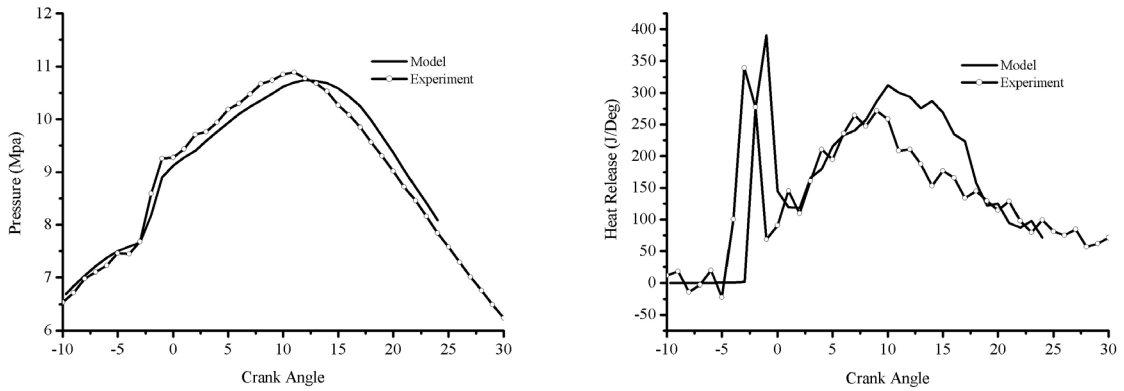

Figure 4-11: Cylinder pressure and heat release curves for the old Caterpillar engine using the PDF time-scale model with a one-equation viscosity based LES turbulence model

It is seen that the pressure and heat release are in reasonable agreement with experimental values. The combustion model captures the major aspects of the combustion process in this case. Temperature contours inside the cylinder in a plane passing through the spray are shown in figure 4-12 for simulations using both a RANS turbulence model as well as the one-equation viscosity based model.

The LES model predicts higher peak temperatures than the RANS model and predicts small regions of high temperature while the RANS model predicts larger regions of high temperature. This is because the added viscosity in RANS models tends to smooth out gradients whereas structure is retained in LES models. It can also be seen that the spray droplet distribution is slightly different for the RANS case and the LES case. However, the differences seen in figure 4-12 are generally not large. This issue is addressed in the next section when a full 360° mesh is used.

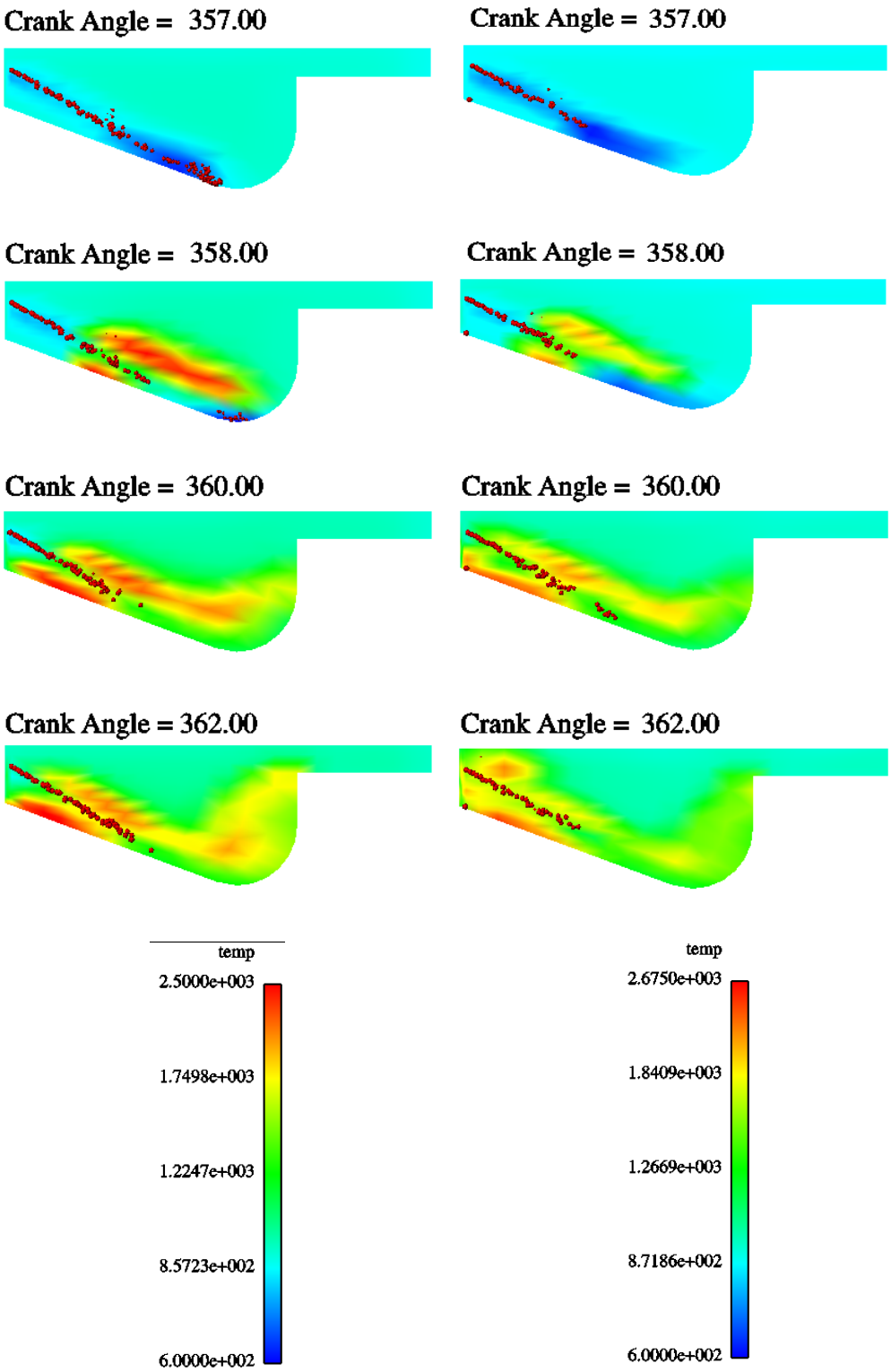

Figure 4-12: Temperautre contours for RANS (left) and the one-equation LES (right) models

4.2.2.3 Dynamic Structure LES model

The third LES model implemented into the KIVA code was the dynamic structure model (Pomraning, 2000). This model was tested for a reacting gaseous jet and was used to simulate engine flow and combustion. The old Caterpillar engine was simulated at the baseline operating condition and the Sandia engine was simulated for the operating condition shown in table 4-1.

Cylinder pressure and heat release as a function of crank angle for these simulations along with experimental data are shown in figure 4-13.

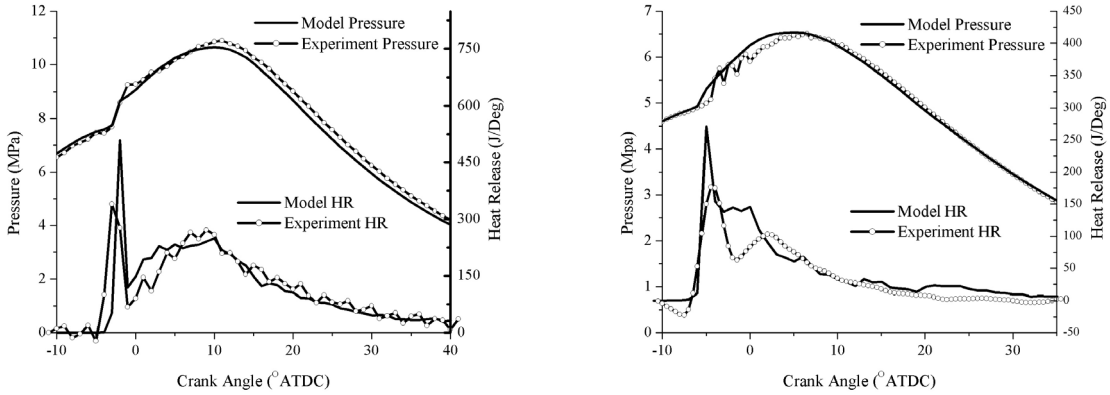

Figure 10: Cylinder pressure and Heat Release for old Caterpillar (left) and Sandia (right) engines using the PDF time-scale model with the Dynamic Structure LES model

The pressure and heat release curves are in good agreement for both engines. The combustion model is able to correctly predict the phasing of the pressure rise and fall and the sharp rise in pressure due to the premixed burn.

The constant C_k in equations **(2-34)** and **(2-37)** for the scalar transport coefficient had to be changed from 0.05 to 0.3 for these cases. This was required because a 60º-sector mesh with periodic boundary conditions was used. Since the periodic boundaries are close to each other near the nozzle tip in the sector mesh, large eddies cannot be formed in this region and large-scale turbulent mixing is suppressed. In order to compensate with sub-grid mixing, additional viscosity is added by increasing the scalar transport coefficient.

In order to test the models in a complex geometry and to avoid the problem of eddy suppression due to irregularities in the mesh, a 360° - Cartesian mesh with intake and exhaust ports and moving valves was used. Two operating conditions for the new Caterpillar engine were simulated. The operating conditions are shown in table 4-3 and a view of the mesh is shown in figure 4-14.

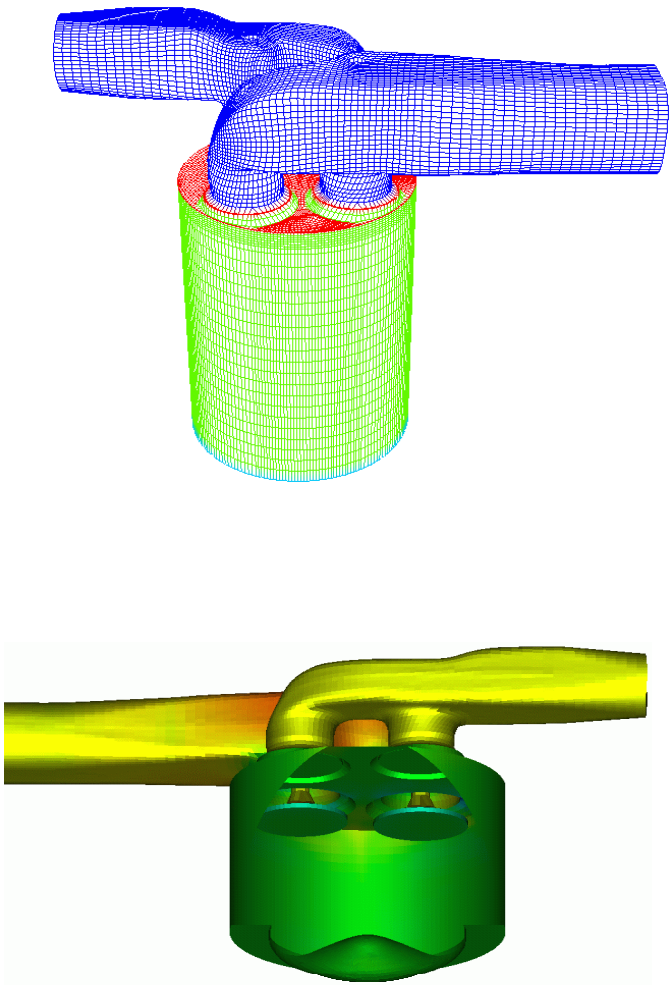

Figure 4-14: New Caterpillar 3401 engine computational grid (approximately 160,000 cells)

Operating Condition	Speed (RPM)	% Exhaust Gas Recirculation	Equivalence Ratio	Fuel Flow rate (g/min)	Injection timing (°ATDC)
Baseline	1737	0	0.4	117.2	-5.5
EGR	1737	6.7	0.44	118.4	-5.5

Table 4-3: Operating Conditions for the new Caterpillar engine

These simulations were started 0.5 crank angle degrees before the intake valve opened and were run until 0.5 degrees before start of injection. At this time, the cylinder

temperature was adjusted to 930 K for the baseline case and 950 K for the EGR case. It was necessary to adjust the temperature to match the mass trapped inside the cylinder. The simulations were then restarted and run until end of combustion. The cylinder pressure for the baseline case is shown in figure 4-15.

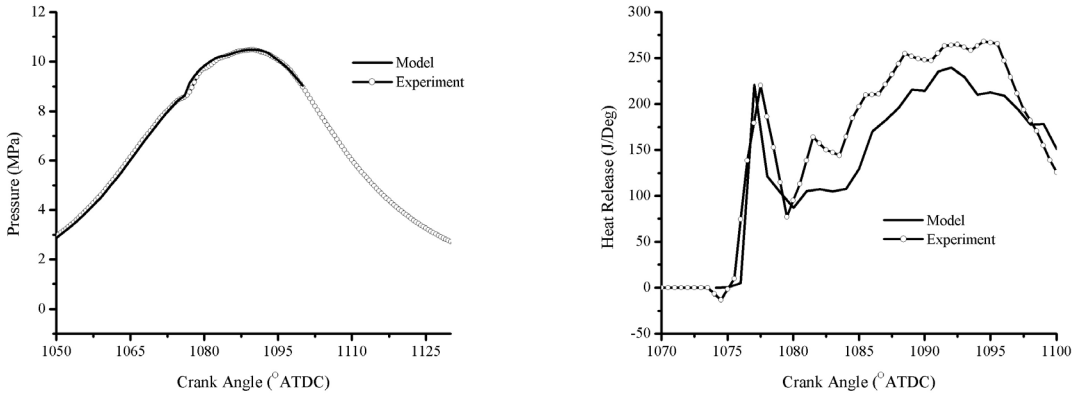

Figure 4-15: Cylinder Pressure and Heat Release for the new Caterpillar engine operating at the baseline condition

It can be seen that as with other models, this model also matches the cylinder average pressure and heat release very well. In this case, it was not necessary to change the constant, C_k as the 3-dimensional nature of the grid allowed the formation of large-scale structures, which allow the turbulent mixing to be represented correctly. This can be visualized by comparing the temperature contour and spray droplet pattern for this simulation with the one performed using the 60° sector mesh as seen in figure 4-16.

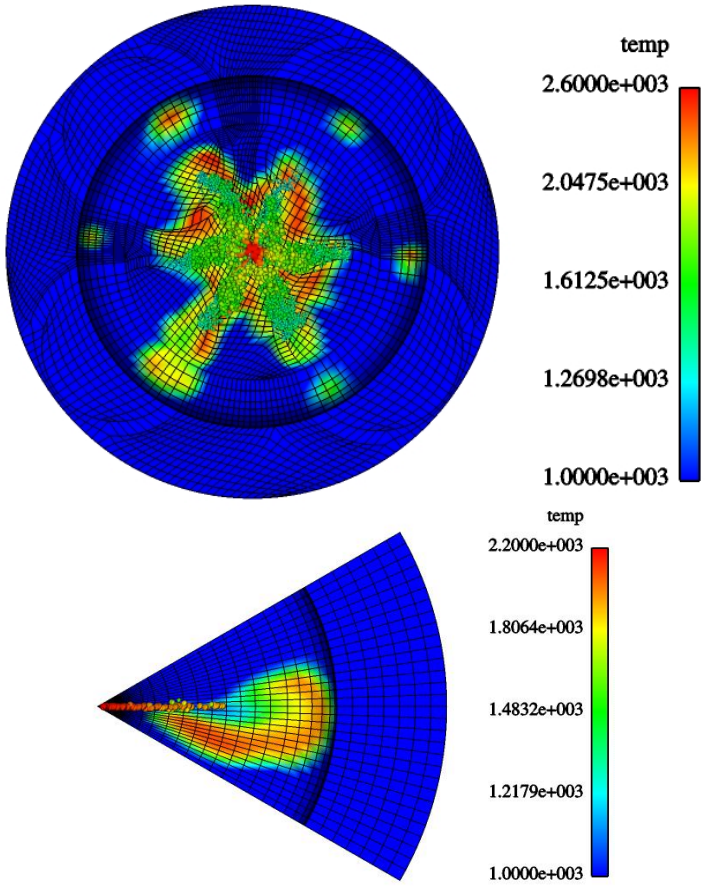

Figure 4-16: Temperature contours and spray distribution for simulations with a 360° Cartesian mesh (new Caterpillar engine) and a 60° sector mesh (old Caterpillar Engine)

More evidence of large-scale structure is seen in results from the 360º Cartesian Mesh than in results from the 60º Sector Mesh. The lack of symmetry in droplet distribution for the six spray plumes and in the temperature distribution around these spray plumes is evident when using the Cartesian mesh with the dynamic strucutre LES model. This indicates that the fuel vapor spreads in a non-symmetric manner in the combustion chamber. The simulation using the sector-mesh shows approximately a symmetric distrubution of temperature around the spray plume. This is not totally symmetric because of the swirl present in the cylinder. Changing the constant, C_k, has the effect of added viscosity and this tends to smear out flow structure.

To verify that the combustion model was working consistently with the turbulence model, another operating condition for the new Caterpillar engine was simulated (table 4-3). Cylinder pressure for that simulation is shown in figure 4-17.

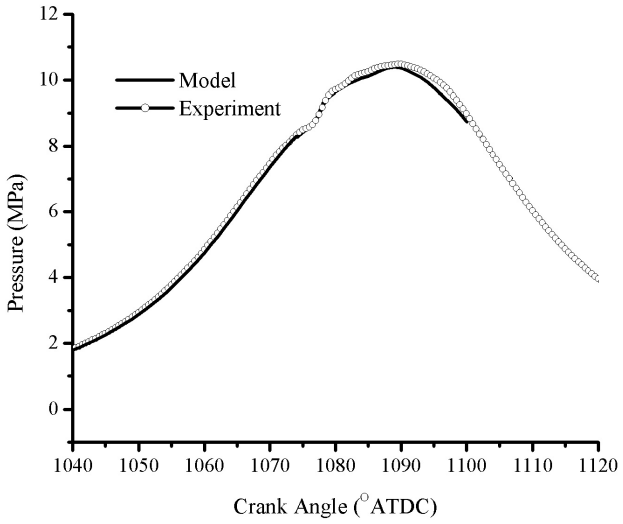

Figure 4-17: Measured and Simulated Pressure for the new Caterpillar engine operating with EGR.

While the simulated pressure agrees reasonably with the experimental value, it starts dropping below the measured value after reaching the peak pressure. This could indicate that the combustion model and mixture fraction need modification due to the presence of EGR. This points to the need to work on making the model consistent for use with cases where EGR is present.

Chapter 5 - Conclusions and future work

References

Lee Daniel, 1999, PhD Thesis, University of Wisconsin - Madison